EUROPEAN ORGANIZATION FOR NUCLEAR RESEARCH

CERN-SPSC/99-35
SPSC/P315
15 November, 1999

Proposal to study hadron production for the neutrino factory and for the atmospheric neutrino flux

M.G. Catanesi, M.T. Muciaccia, E. Radicioni, P. Righini, S. Simone
Università degli Studi e Sezione INFN, Bari, Italy

I. Boyko, S. Bunyatov, G. Chelkov, D. Dedovitch, P. Evtoukovitch, L. Gongadze, G. Glonti, M. Gostkin, S. Kotov, D. Kharchenko, O. Klimov, Z. Kroumchtein, Y. Nefedov, M. Nikolenko, B. Popov, I. Potrap, A. Rudenko, E. Tskhadadze, V. Serdiouk, V. Zhuravlov.
Joint Institute for Nuclear Research, JINR Dubna, Russian Federation

M. Doucet, F. Dydak*, J-P. Fabre, A. Grant, L. Linssen, J. Panman, I.M. Papadopoulos, F.J.P. Soler, P. Zucchelli
CERN, Geneva, Switzerland

R. Edgecock
Rutherford Appleton Laboratory, Chilton, Didcot, UK

A. Blondel[1]
Section de Physique, Université de Genève, Switzerland

U. Gastaldi
Laboratori Nazionali di Legnaro dell'INFN, Legnaro, Italy

G. Gregoire
UCL, Louvain-la-Neuve, Belgium

M. Bonesini, M. Calvi, S. Gilardoni, M. Paganoni, A. Pullia
Università degli Studi e Sezione INFN, Milano, Italy

S. Gninenko, M. Kirsanov, Yu. Musienko, A. Poljarush, A. Toropin
Institute for Nuclear Research, Moscow, Russia

V. Palladino
Università "Federico II" e Sezione INFN, Napoli, Italy

M. Baldo Ceolin, F. Bobisut, D. Gibin, A. Guglielmi, M. Laveder, M. Mezzetto
Università degli Studi e Sezione INFN, Padova, Italy

J. Dumarchez, F. Vannucci
Université de Paris VI et VII, Paris, France

U. Dore
Università "La Sapienza" e Sezione INFN, Roma, Italy

M. Chizhov, D. Kolev, R. Tsenov
Faculty of Physics, St. Kliment Ohridski University, Sofia, Bulgaria

G. Giannini, G. Santin
Università di Trieste e Sezione INFN, Trieste, Italy

A. Cervera-Villanueva, J. Diaz, A. Faus-Golfe, J.J. Gomez-Cadenas, M.C. Gonzalez-Garcia, J. Velasco
University of Valencia, Valencia, Spain

P. Gruber
Institut für Kernphysik, Technische Universität, Wien, Austria

*contact-person
[1]now at Ecole Polytechnique, Palaiseau, France

Contents

1 Introduction and summary

It is proposed to carry out at the CERN PS a programme of measurements of secondary hadrons, over the full solid angle, produced on thin and thick nuclear targets by beams of protons and pions with momentum in the range 2 to 15 GeV/c.

The main motivation is twofold: to acquire adequate knowledge of pion yields for an optimal design of the recently proposed intense neutrino source based on muon decay in a muon storage ring (neutrino factory); and to improve substantially the calculation of the atmospheric neutrino flux which is needed for a refined interpretation of the evidence for neutrino oscillation from the study of atmospheric neutrinos in present and forthcoming experiments.

Additional motivations are: a measurement of the yield of low-momentum backward-going pions which could be used for a high-intensity stopped-muon source as a by-product of the neutrino factory; and a better precision of the fluxes in conventional neutrino beams such as at the KEK 12 GeV/c proton-synchrotron, important for the K2K experiment, and at the low-energy (8 GeV/c) booster at Fermilab, used for the MiniBooNe experiment.

A neutrino factory requires a sophisticated front-end: the proton target, pion capture, pion phase rotation, pion decay, muon capture, and muon cooling. Existing data on the overall yield and distribution in phase space of pions produced in low-energy proton–nucleus collisions are not adequate for a quantitative and optimized design. For the proton source, several options as diverse as a 2 GeV/c proton linac and a 16 GeV/c rapid-cycling synchrotron are under discussion. Deuterons, which provide more symmetric yields of positive and negative pions than protons, are discussed as an alternative to protons. As in the case of a 2 GeV/c proton linac the largest pion yield is expected for pions with momentum $\sim$ 200 MeV/c, the proposed experiment aims at the identification and measurement of pions down to momenta well below 100 MeV/c.

The existing $\sim$ 30% uncertainty in the calculation of absolute atmospheric neutrino fluxes and the $\sim$ 7% uncertainty in the ratio of neutrino flavours could be substantially reduced by measuring the spectrum of positive and negative pions produced by protons in the full range of PS beam momenta. This is relevant for the interpretation of current results from SuperKamiokande [1, 2] and even more so for future atmospheric neutrino experiments which are expected to make use of atmospheric neutrinos down to an energy of 100 MeV. Also, pion production by helium nuclei is important, as helium nuclei constitute $\sim$ 10% of the primary charged-particle cosmic-ray flux. Existing data are mostly from single-arm hadron production experiments [3, 4] which were carried out in the seventies. Present models and computer generators of hadron production in proton–nucleus collisions in the atmosphere have been tuned to describe these data. However, the scale error in these experiments was estimated at 15% or more, mostly arising from acceptance uncertainties. In addition, at low momenta where different models for pion production on nuclei make very different predictions of atmospheric neutrino fluxes, experiments either did not provide any data at all or lacked particle identification capable of separating pions from protons.

The E910 experiment at BNL [5] took data in 1996 which will be relevant to some of the issues mentioned above. The experiment's goal was the study of strange matter production by protons on nuclei, with a view to making a comparison with nucleus–nucleus collisions. First papers on 'centrality' measurements were published recently [6]. There is overlap between E910 and the proposed experiment at high proton momenta, as E910 took data at proton momenta of 6, 12 and 18 GeV/c. The 6 GeV/c data have low statistics. No data were taken with thick targets.

The proposed experiment comprises a large-acceptance charged-particle magnetic spectrometer of conventional design, located in the East Hall of the CERN PS and using the T9 tagged

charged-particle beam. It will re-use existing equipment as much as possible, notably from the NOMAD [7] and CHORUS [8] experiments. Of particular importance is the re-use of the ALEPH prototype TPC [9], albeit with substantial modifications. The only major piece to be newly built is a threshold Cherenkov detector with gas at atmospheric pressure.

It is planned to have a technical run in the end of 2000, and the physics run in 2001. For the year 2002, a second phase of the experiment is under discussion [10] with a view to removing the primary proton target and sending deuterium and helium nuclei directly to the target of the experiment.

Although the dominant uncertainties in the atmospheric neutrino fluxes will be removed by the proposed experiment, an extension to higher beam momenta in a third phase, up to ~ 100 GeV/c, could be contemplated, including running with helium ions. Such a program would not only extend reliable calculations of atmospheric neutrino fluxes into the 100 GeV/c region, but also contribute to solving the puzzle of the 'knee' of the charged-particle cosmic-ray spectrum around 3×10^{15} eV. Progress in this area is hampered no longer by the lack of availability of good data, but by their interpretation in terms of atmospheric shower models. Such models not only need better experimental input on the interaction of the very high-energy primaries, but also on the interactions of lower-energy secondaries with oxygen and nitrogen. It is with respect to the latter aspect that this experiment can provide useful input.

Certain measurements with higher beam momenta are within reach of the COMPASS experiment at the SPS.

2 Physics motivation and goals

2.1 Neutrino factory

A neutrino factory is a complex machine to produce neutrinos from circulating muons decaying in a storage ring [11]. Controlling the muon-beam characteristics will allow a well collimated ν beam of high intensity and high energy to be obtained. The aim is to achieve intensities of 10^{20} to 10^{22} μ per year in the decay ring. The highest conventional neutrino flux is currently planned for the MINOS near detector with 10^{18} ν_μ and 5×10^{15} ν_e per year [12].

The generic layout of a neutrino factory (see Fig. 1) consists of a proton accelerator, a target and a muon storage ring [13]. A high power (4 MW) proton beam impinges on a target producing pions which are collected with a high magnetic field. In a drift space, they decay into a muon and a muon neutrino that is lost ($\pi^+ \rightarrow \mu^+ + \nu_\mu$). After this, the muon phase space is reduced with ionization cooling, the muons are accelerated to energies of up to 50 GeV and fed into a decay ring where they decay into an electron/positron and two neutrinos ($\mu^+ \rightarrow e^+ + \nu_\mathrm{e} + \overline{\nu}_\mu$). The muons decaying in the straight sections of this ring produce a high intensity neutrino beam that points towards a neutrino detector, allowing neutrino oscillation experiments with high precision. By changing the sign of the charge of the collected pions it is possible to get the two conjugated neutrinos, $\overline{\nu}_\mathrm{e} + \nu_\mu$.

2.1.1 Pion production in a neutrino factory

In this context, accurate pion production yields are very important to achieve the desired neutrino fluxes and to design a cost-effective machine [14]. The design goal is to maximize the figure

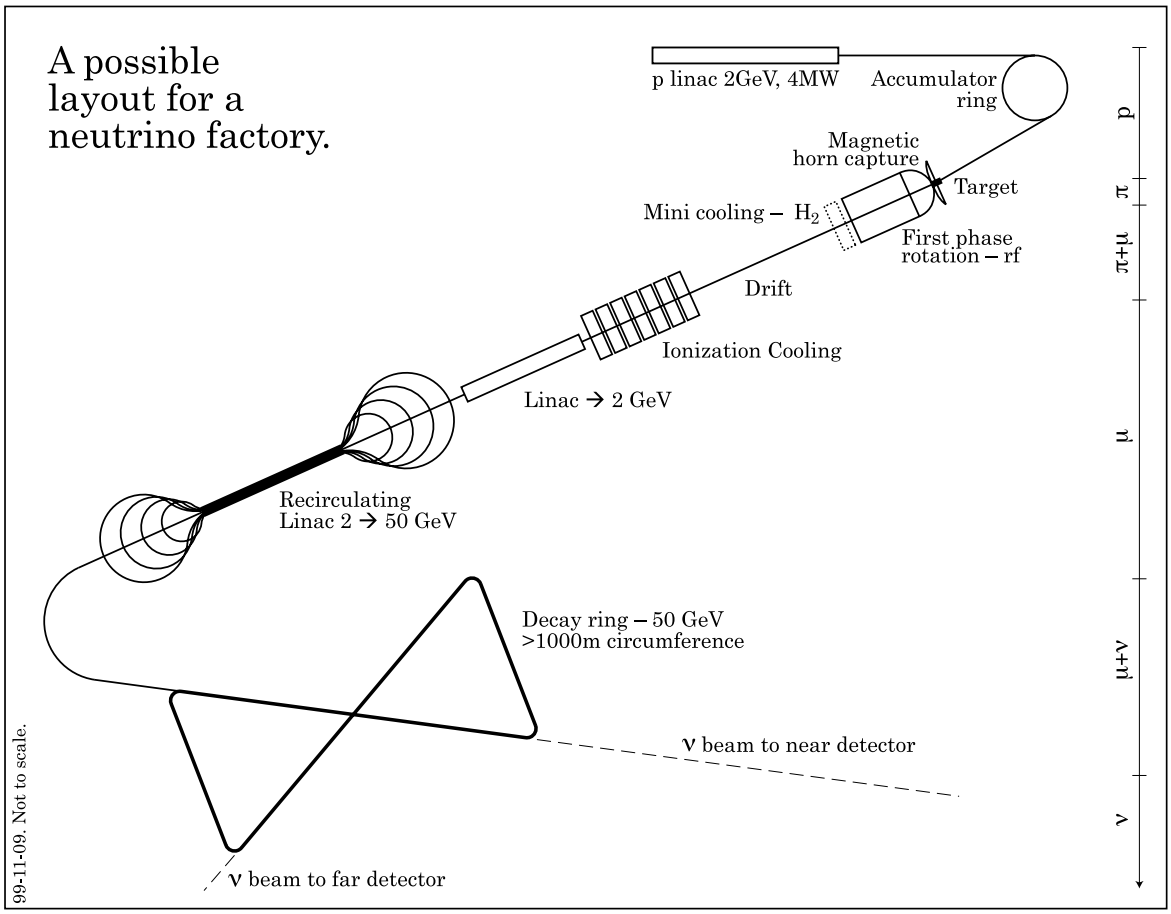

Figure 1: Generic Layout of a Neutrino Factory.

of merit, which is the number of accelerated muons in the decay ring of each sign. The time for measuring a certain number of events in an oscillation experiment should be minimized, thus the goal is to maximize both pion production rates. With the pion production rate per proton per unit of energy $r_\pi = n_\pi/(n_\mathrm{p} \cdot \mathrm{GeV})$ we get the expression to be minimized:

$$\frac{1}{r_{\pi^+}} + \frac{1}{r_{\pi^-}}. \tag{1}$$

Current simulations of the pion yield with FLUKA and MARS show a 30%–100% discrepancy in the pion production [15]. It is reasonable to assume a similar uncertainty for the momentum distribution. The reason for this uncertainty is the small amount of underlying experimental data for the simulation programs. A high-precision pion production experiment would thus be a requirement for the simulation of a neutrino factory.

2.1.2 Parameters

The variables affecting the pion production are proton energy, target material and target geometry (diameter and length). The total proton-beam power is only a scaling parameter. A pion production experiment should give the set of data necessary to optimize both proton energy and target material in order to achieve the highest number of potentially collected pions *of both charge signs* per unit of energy.

Table 1: Proposed proton drivers [13].

		CERN	CERN BNL	FNAL	JHF
		Linac + Accumulator	Synch.	Synch.	Synch.
Proton momentum	GeV/c	2	24	16	50
Repetition Rate	Hz	50	5	15	2.5
Proton beam Power	MW	4	4	4	4
Number of protons per pulse	10^{14}	1.3–2.6	2	1	2

Table 2: Desired parameters of the experiment.

Parameter	Range
Proton momentum	2–24 GeV/c; 1–2 GeV/c steps
Angular acceptance	4π
Target thickness	thin, 1 and 2 interaction lengths
Target materials	Li, Be, C, Al, Ni, Cu, liq. Ga-Sn, W, liq. Hg

A list of proton drivers under consideration in different laboratories is given in Table 1. They are all based on upgrades of existing machines, except the CERN scenario of a 2 GeV/c linac that could be based on super-conducting LEP cavities.

Several target materials have been proposed, starting from low-Z materials such as Be and Li over C to high-Z materials such as Ni, Cu, liquid Hg, or W. In addition, deuterium has been proposed as target material for a recirculating proton scheme [16]. Apart from efficient pion production, cooling the target is a major concern in choosing the right material. Estimates show that, depending on the proton energy, up to 30% of the proton power is dissipated in the target and has to be cooled. Even though the proposed experiment is a low-intensity one, hints on the energy deposition in the target can give valuable information to design the target-cooling subsystem. A list of the desired experimental parameters is shown in Table 2.

2.1.3 Desired experimental data

The data taken in the experiment will be used to validate the design of the neutrino factory downstream the target. The transverse capture and the first phase rotation are strongly dependent on the pion production data. The transverse momentum distribution of the pions must be known to a high precision as it affects the efficiency of transverse capture. At first sight the longitudinal momenta are not required to be known with such an accuracy, as a wide range of them will be captured. Although this argument is valid for capture, this is not the case for the first phase rotation where the pion beam is nearly mono-energetic (in order to distinguish between forward- and backward-decaying pions for enhanced polarization of the muon beam). A high precision on the longitudinal momentum is therefore also necessary.

The overall pion yield per incident proton will be a scaling parameter for the figure of merit of the neutrino factory. A precision of 5% in the pion yield will be sufficient. The same accuracy is required for the ratio of π^+ to π^-, as the particle with lower production yield determines the proton-beam power needed. The desired data to be taken in the experiment are shown in

Table 3: Desired data.

Parameter	Range	Precision
π longitudinal momentum	100–700 MeV/c	< 25 MeV/c
π transverse momentum	0–250 MeV/c	< 25 MeV/c
Number of secondary π/proton		5%
π^+/π^- ratio		5%

Table 3.

2.2 Atmospheric neutrino flux

The SuperKamiokande collaboration has presented evidence for neutrino oscillation based on a high-statistics sample of atmospheric neutrino interactions [1, 2]. The detailed interpretation of these data, as well as the comparison with measurements at different locations and with different techniques, requires reliable calculations of fluxes of atmospheric neutrinos.

Several one-dimensional calculations of the flux of atmospheric neutrinos have been published [17, 18, 19, 20]. Recently, more sophisticated three-dimensional calculations have become available [21, 22]. However, it has been claimed by Battistoni et al. [21] that for practical purposes the one-dimensional calculations give adequate results. Therefore, it makes sense to include both one- and three-dimensional calculations in the comparison of the results of different calculations. The various calculations quote large errors and differ significantly in their results. These differences have attracted quite some attention and have been extensively analyzed [23, 24, 25]. The dominant sources of discrepancies were found in

- the assumed energy spectrum and the chemical composition of the primary cosmic rays; and
- the representation of pion production in collisions of the primaries with nitrogen and oxygen nuclei.

Next in the order of uncertainties is the neutrino-nucleon cross-section, which is surprisingly uncertain at low energy. Ultimately, measurements in so-called 'near' detectors at the neutrino factory will entirely eliminate this latter source of error.

There used to be sizeable (up to 30%) differences between measurements of the primary flux; however thanks to several new measurements [26, 27, 28] there is a tendency toward convergence, and hopes are that with a new round of long-duration balloon flights this uncertainty will be reduced and will become insignificant within a few years. This leaves the representation of pion production on light nuclei as the only remaining major obstacle to a precise (i.e. few per cent) calculation of the atmospheric neutrino flux in contrast to its current uncertainty of $\sim 30\%$ for neutrino energies $E_\nu < 10$ GeV.

For lower-energy neutrino events such as the 'sub-GeV' sample of SuperKamiokande, the parent cosmic-ray primaries have energies in the range 5–100 GeV as shown in Fig. 2 taken from Ref. [29].

For the atmospheric neutrino flux, the overall yield of pions is all-important, integrated over the full phase space. The value of measurements therefore depends on the overall normalization

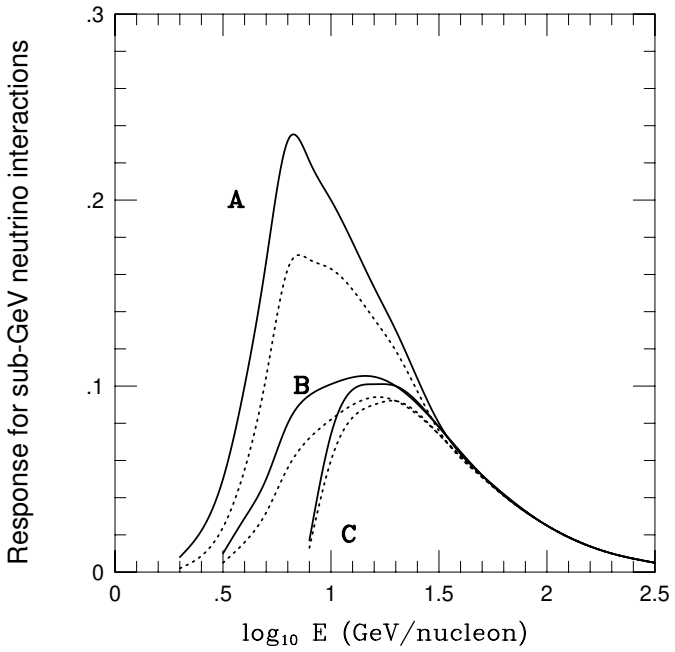

Figure 2: Response for 'sub-GeV' neutrino events in SuperKamiokande to the energy of cosmic-ray primaries. Curve A: no geomagnetic cut-off; Curve B: events from below; Curve C: events from above. Each pair of curves gives the range of solar activity between minimum (solid) and maximum (dotted).

precision of the experiment, and on its phase-space coverage.

To illustrate the problem, Fig. 3 taken from Ref. [29] shows the fraction of the phase space which falls inside the acceptance of various experiments measuring pion production by protons on beryllium [3, 4, 30]. The unmeasured regions have to be covered by extrapolation guided by models of pion production.

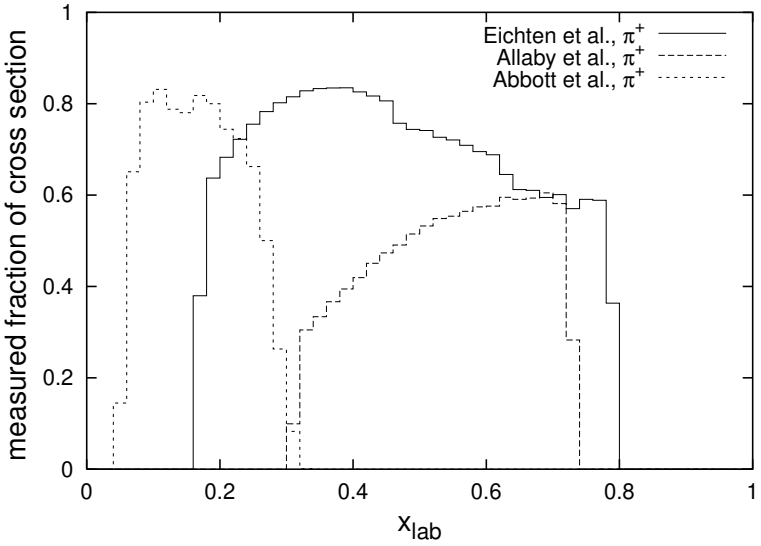

Figure 3: Fraction of pion production cross-section covered by different pion production experiments in p–Be interactions.

To the uncertainty in this extrapolation other sources of uncertainty have to be added. The overall normalization error of the experiments was typically 15%. The lack of data on nitrogen-like nuclei makes necessary yet another extrapolation from beryllium data. Finally, it is to

be recalled that $\sim$ 15% of the primary cosmic-ray nucleons are bound in helium nuclei and measurements of production yields from their interactions with oxygen and nitrogen nuclei are not available.

The conclusion from the above discussion is that a single high-precision large-acceptance production experiment is needed which measures pion production by protons and helium nuclei on nitrogen and oxygen targets. With these data in hand, in a few years time, the event rate from atmospheric neutrinos will be calculable with a few per-cent precision.

2.3 Scope of the experiment

2.3.1 What is required?

The design considerations of the neutrino factory require the following measurements:

- Proton beam with momentum between 2 and 24 GeV/c.
- Thick high-Z targets. However, since the proton target of the neutrino factory is in a very high magnetic field, its final efficiency for pion production will be determined from a combination of thin- and thick-target measurements, and calculations. The calculated thick-target yield in a non-magnetic environment is checked by measurement.
- Secondary pion yield over the phase space: 100 MeV/c $< p_{\mathrm{L}} <$ 700MeV/c and $p_{\mathrm{T}} <$ 250MeV/c; secondary proton yield to assess problems of induced radiation.
- Deuterium beams with momentum of 1 GeV/c per nucleon to assess its usefulness for a better π^+ /π^- ratio than obtained with a proton beam.
- Yield of backward-going pions to assess its usefulness for a high-intensity stopped-muon source.

For a reliable calculation of the atmospheric neutrino flux down to 100 MeV energy, the following measurements are needed:

- Proton and pion beam with momentum between 1 and 100 GeV/c.
- Targets of oxygen and nitrogen nuclei.
- Secondary π^+, π^-, K^+, K^- and proton yields over the full phase space, with particle energy as the kinematical quantity of primary interest. The precision requirement is a few per cent for π^+, π^- and proton, and $\sim$ 10% for kaons.
- Helium ions with momentum between 0.5 and 50 GeV/c per nucleon to complement the proton data.

In the context of atmospheric neutrinos, it should be recalled that the measurement precision of the π^0/e ratio in SuperKamiokande, which is relevant for the question whether a sterile neutrino is required, depends on the precision of the measurement of the π^0 production via neutral currents in the K2K experiment at KEK. This experiment is in turn limited by the knowledge of pions and kaons produced by 12 GeV/c protons on a thick Al target. The results of the proposed experiment would be instrumental in achieving a better precision on this important cross-section.

The MiniBooNe experiment at Fermilab would also benefit from precision measurements of 8 GeV/c protons on a thick Al target. This experiment aims to refute or confirm the LSND neutrino oscillation claim.

2.3.2 What is experimentally possible?

The two main constraints of the proposed experiment are the available beam momenta of the T9 beam line in the East Hall, which is limited to 15 GeV/c and the need to re-use existing equipment as much as possible, with a view to gaining time and minimizing capital expenditure.

Altogether, the following scenario emerges:

- Stage 1: T9 beam in the East Hall with proton and pion beams in the range 2–15 GeV/c; several thin targets spanning the full range between Be and W nuclei; a selection of thick targets.
- Stage 2: T9 beam line in the East Hall, with the primary proton target removed, and dedicated PS running with deuterium and helium beams at selected momenta. Additional targets.
- Stage 3: An experiment at the SPS with a secondary beam momentum between 15 and 100 GeV/c as well as with deuterium and helium beams at selected momenta. It is expected that COMPASS has the potential to perform some of these measurements.

At this point in time, approval is sought for Stage 1 only.

2.3.3 Precision requirements

Both for the neutrino factory and for the atmospheric neutrino flux, an overall precision of 2% for the inclusive cross-section of secondary particles is the primary aim. This is motivated by the wish to obtain 5% precision both on the production of accepted muons in the neutrino factory's front stage, and on the atmospheric neutrino flux. Either prediction will involve uncertainties beyond those of the results of the proposed experiment.

A 2% overall accuracy requires some 10^4 events for each measured point, of which there are many. It will take several months of running time to achieve sufficient statistical precision (see section 4).

Acceptance calculations are potentially more precise with modern simulation tools than previously, when typically a 10% precision was considered satisfactory. The largest challenge comes from understanding efficiencies with an error of order 1%. This calls for as much redundancy as can be afforded, with a view to cross-calibrating efficiencies. For example, pion/proton identification is provided by $\mathrm{d}E/\mathrm{d}x$ in a Time Projection Chamber (TPC), by time of flight (TOF), and by a threshold gas Cherenkov detector. Overlap in certain kinematical domains will help to understand absolute efficiencies.

2.4 Particle identification

At different energies, the purity of the pion sample is affected by different backgrounds, as can be seen in the following two extreme conditions:

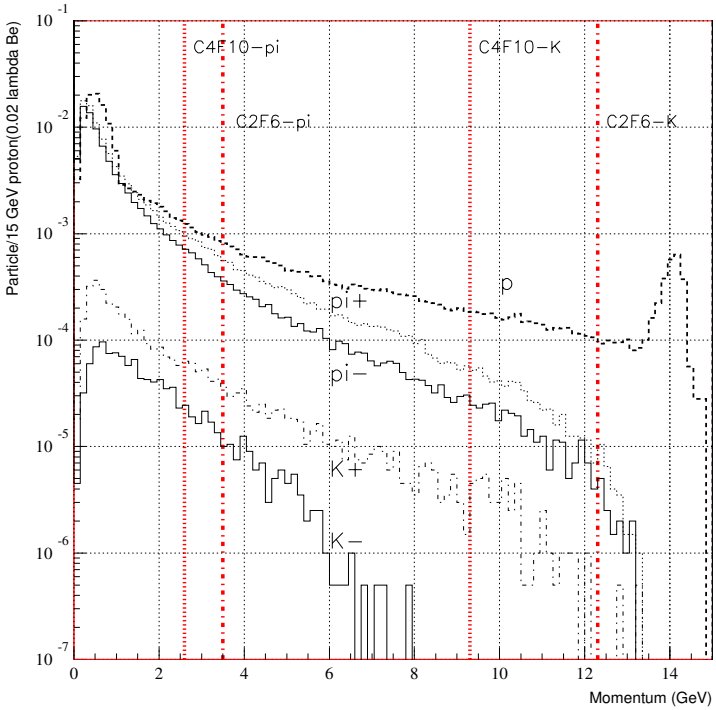

Figure 4: Kaon, pion and proton spectra for a 15 GeV/c proton incident beam on a 2% interaction length Be target. Elastic proton scattering is not included. Vertical lines indicate Cherenkov threshold values for pions and kaons with different gases.

- At 2 GeV/c incident proton momenta, no kaons can be produced. However, the scattered proton flux has been estimated (GFLUKA) to be about 4.7 times larger than the π^+ rate (thin targets) when integrated over all possible momenta. Despite the differences in the p_{T}–p_{L} distribution, the pion identification requires a powerful proton rejection bigger than a factor ~ 100.

- With a 15 GeV/c proton beam, the integrated p/π^+ ratio is about 1.4, and the same quantity for K/π^+ is $\sim 1.1 \times 10^{-2}$. As shown in figure 4, both values are larger in the high energy region, and for example amount to $\mathrm{p}/\pi^+ \sim 4$ and $\mathrm{K}^+/\pi^+ \sim 0.1$ at 10 GeV/c. Therefore the measurement of the π^+ flux with the required accuracy implies a particle identification capable of a large proton suppression as at 2 GeV/c and in addition a $\sim 2\sigma$ rejection of the kaon component.

The experiment plans to exploit three different methods of particle identification: for low momenta by $\mathrm{d}E/\mathrm{d}x$ in the TPC, complemented by TOF measurement; for high momenta by a threshold Cherenkov counter filled with C_4F_{10} at atmospheric pressure complemented by $\mathrm{d}E/\mathrm{d}x$ in the TPC in the relativistic rise region.

The TPC drifts the charge deposited by ionizing tracks in the Ar–CH_4 gas volume towards a multi-anode proportional-wire plane and measures the charges induced on pads located 4 mm from the anode wires. With a 5 MHz clock frequency and a drift velocity of 5 cm per μs, the deposited primary charge is sampled every cm parallel to the TPC axis. Since the target is located at a depth of 50 cm from the upstream end of the TPC, the maximum number of samplings for small-angle tracks is 90. For large-angle (90°) tracks, the number of samplings is limited by the number of concentric pad rings, which is 21. The $\mathrm{d}E/\mathrm{d}x$ measurement in the TPC is expected to have a resolution of $\sim 6\%$.

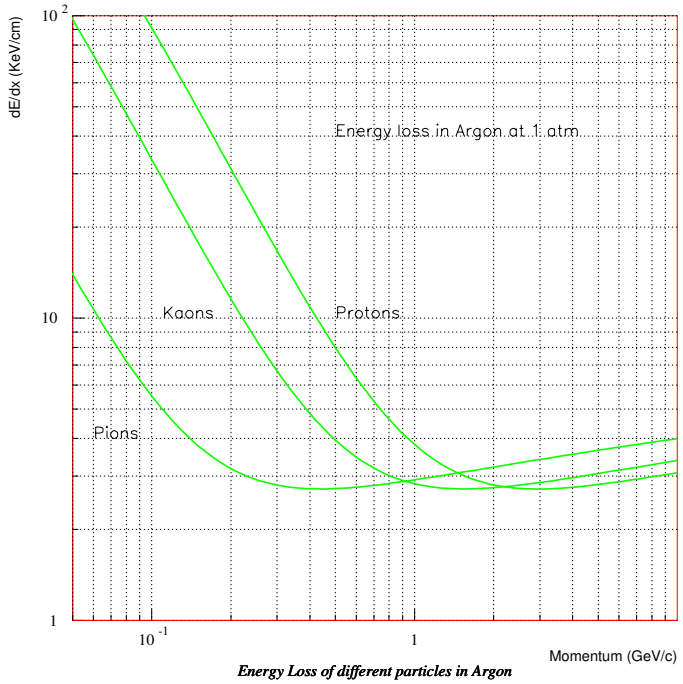

Figure 5: Ideal $\mathrm{d}E/\mathrm{d}x$ measurement in the TPC as a function of momentum, for pions, kaons and protons. No measurement smearing has been included. The density parameter has been neglected.

By virtue of the momentum-dependence of the specific ionization, $\mathrm{d}E/\mathrm{d}x$, of different particle species, particle identification is possible for certain ranges of momentum. The $\mathrm{d}E/\mathrm{d}x$ for pions, kaons and protons is shown in Fig. 5. Up to ~ 0.7 GeV/c momentum, pions are well separated from kaons, and up to ~ 1.2 GeV/c from protons. Kaons are well separated from protons up to ~ 1.5 GeV/c, but cannot easily be distinguished from protons above this momentum. However, pions can be distinguished from protons in the region of the relativistic rise, above 3 GeV/c. A more complete analysis is reported in section 6.2.

A TOF with sufficient flight path and good timing adds welcome redundancy to particle identification in the TPC. Figure 6 shows the difference in time of flight for pions with protons and kaons as a function of the momentum, for a flight path of 10 m. If a resolution of 300 ps is assumed a 2σ separation between pions and protons (kaons) is possible up to 4.6 GeV/c (2.4 GeV/c) for a flight path of 10 m. For the π/p distinction a 4σ separation is achieved up to 3.5 GeV/c.

The most relevant range for the TOF is $p < 3.0$ GeV/c, since a gas threshold counter can separate pions from kaons and protons for momenta above 3.0 GeV/c. A gas Cherenkov filled with C_4F_{10} would have a threshold for pions at 2.5 GeV/c and for kaons at 9 GeV/c, thus allowing the positive identification of pions in the complete range of interest. The velocity of the different particles as a function of the momentum is shown in Fig. 7.

In conclusion, the combination of the TPC, the TOF and the gas Cherenkov counter would provide separation of pions, kaons and protons over a large range of the momenta.

Electrons and muons will also be produced copiously: the former in π^0 decays followed by gamma conversions, or in δ-rays from pions; the latter in pion decays. Both types of particle must be separated from pions. In addition, the muon contamination of the incident beam must be measured.

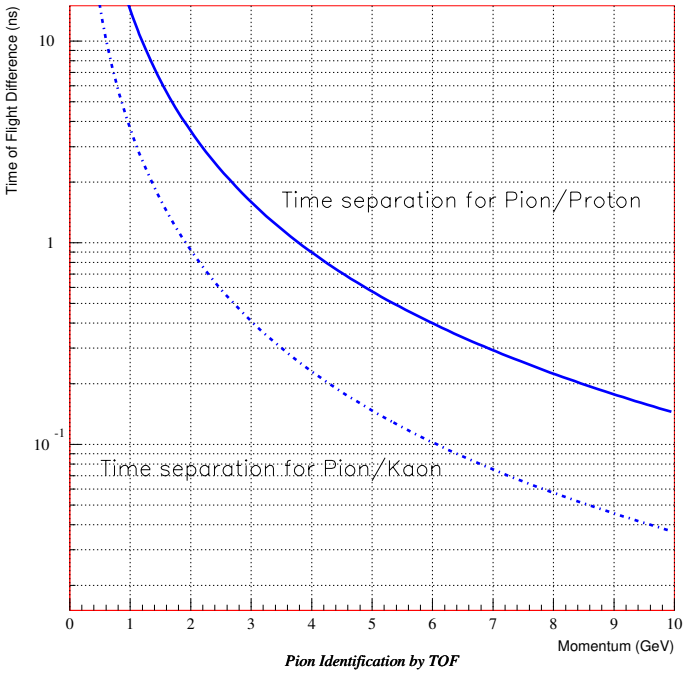

Figure 6: Time of flight difference for pions/kaons and pions/protons as a function of momentum for a flight path of 10 m.

To minimize δ-rays from pions, the amount of material upstream of the gas Cherenkov counter must be kept small.

Genuine high-momentum electrons will be flagged also by 10 X_0 of a lead–scintillating fibre wall far downstream.

Muons will be identified with a sandwich of four times 10 cm of iron, interleaved with scintillating fibres embedded in lead (75% lead) and drift chambers. Muons will thus be flagged by non-interaction in 3.4 $\lambda_{\rm I}$.

3 Experimental setup

3.1 Beam and experimental area

It is proposed to mount the hadron production experiment in the East Hall of the PS in the T9 beam line. This beam will provide charged particles with a good momentum resolution, down to $\sim$ 0.24%, in the range 1.0 to 15.0 GeV/c. No particle separation is possible. As shown in Fig. 8 there is adequate space for an experimental area of 15 $\times$ 20 m^2 behind the ATLAS/CMS test area. It seems desirable to be downstream of this area, because with a mobile beam stopper installed at the end of the test area and in front of our system we will have the maximum flexibility for installation and test of the experimental equipment. There will be no major requests from ATLAS and only a few small-scale beam tests from CMS during 2000 and 2001. During 2002 there may well be requests for the assembly-area floor space for calorimeter assembly and tests; this will need to be resolved.

Apart from the limited maximum momenta of the T9 beam, because of the magnet in the main

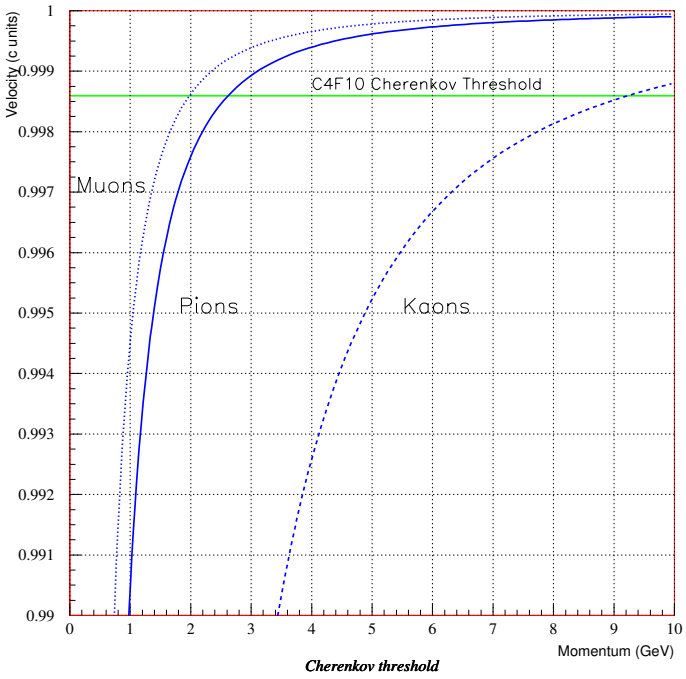

Figure 7: Particle velocities as a function of the particle momentum in the range p GeV/c < 10 GeV/c, together with the threshold for Cherenkov light in C_4F_{10}.

horizontal bend, it is quite suitable for our requirements. The beam length from primary target to the reference focus in the test area is 55.81 m. The flux of protons and pions of a few 10^5 per spill of 2 $\times 10^{11}$ protons on the primary target is adequate. The flux of low-energy kaons is very low due to decays in this long beam line. The typical spill structure of the beam will be a single 400 ms burst each 14.4 s cycle. The horizontal dispersion of the beam is corrected, and a typical momentum bite is 1% for a momentum collimator setting of 4 mm. The vertical dispersion is not corrected and will give some increased size to the beam spot in the target. The extra height of the beam, 2.5 m, is also an advantage for the proposed large detector.

There are two Cherenkov counters in the beam: one 5 m long, permanently installed in the final quadrupole doublet before the reference focus; and another, 3 m long, which can be installed in front of the focus. The Cherenkov counters are not very useful at low energies, because of the large multiple scattering, hence below 2 GeV/c TOF should be used instead.

Some small modifications are required to make a second focus in our area: a doublet of 1.5 m quadrupoles is placed at the end of the test area, with a new evacuated beam pipe and a modified beam stopper which can be quickly removed by the overhead crane. The spot size at our target could be of the order of 5×5 mm^2, but there are still many possibilities for further optimization. The quadrupoles and power supplies are available, the other requirements are small. The design and construction of our target, and the final beam monitoring and trigger will be the responsibility of the collaboration.

The power and water cooling for the TPC and spectrometer magnets are available in the East Hall. There is a single counting room available of about 30 m^2. This is insufficient for the proposed experiment and an additional hut will need to be installed.

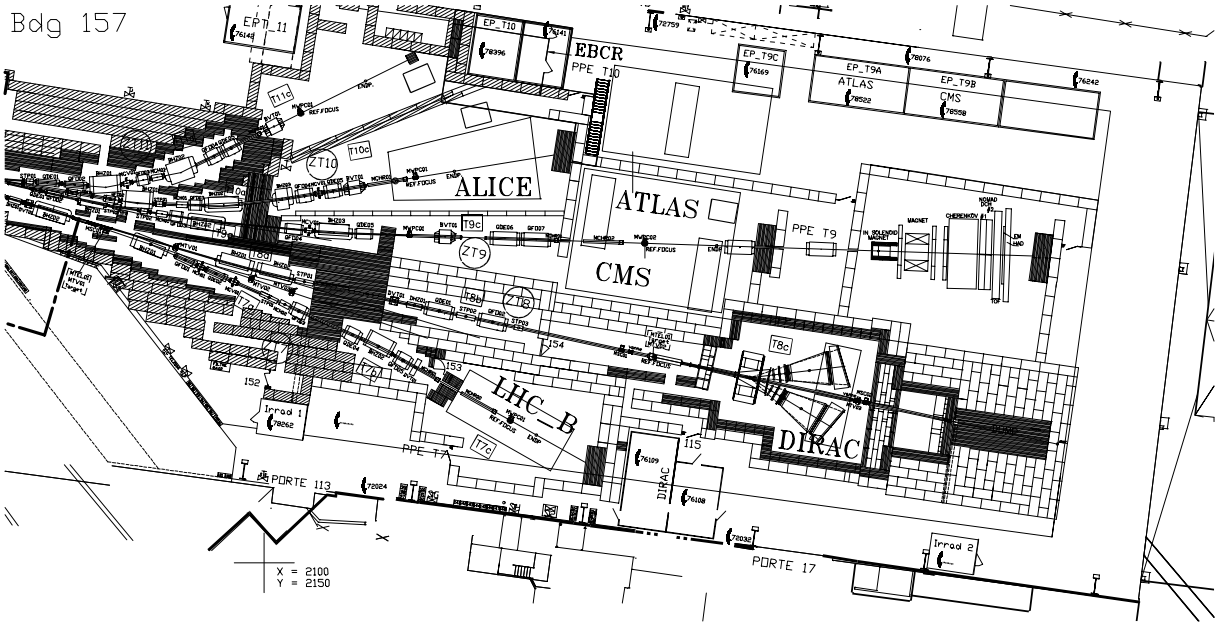

Figure 8: Location of the experiment in the CERN PS East Hall. The proposed experiment is located downstream of the ATLAS/CMS area in the T9 beam line.

3.2 Overview of the spectrometer

Figure 9 shows the plan and elevation views of the experiment. Table 4 lists the various detectors of the spectrometer. The table also summarizes the geometric envelopes of each detector along the beam axis (z-axis). The x-axis is defined to be horizontal, pointing to the right; the y-axis is vertical, pointing downwards. The direction of the incoming particles upstream of the target is measured by two small wire chambers with x and y readout planes. Several scintillation counters for TOF and trigger purposes are placed in the beam line.

The target itself is placed in an insert at a distance of 0.5 m downstream, inside the TPC (see section 3.4. The TPC provides $\mathrm{d}E/\mathrm{d}x$ and momentum measurements of the outgoing particles. It is a 1.5 m long cylinder of 0.9 m diameter surrounded by a 1.5 T solenoid. Trigger counters surround the TPC.

The momentum measurement of the outgoing particles is completed by the downstream spectrometer. It comprises a quadruplet of NOMAD drift chambers before and one such quadruplet after a large-aperture spectrometer magnet with a field strength of 1.0 Tm. All drift chambers measure triplets; they are described in Section 3.6. The spectrometer magnet is described in Section 3.5.

The drift chambers after the magnet are followed by a C_4F_{10} threshold Cherenkov counter, used to provide pion/kaon separation above 2.5–3 GeV/c (see Section 3.7).

Further drift-chamber stacks are followed by a TOF-scintillator double wall placed 10 m from the target (see Section 3.8). The TOF wall provides particle identification below about 4–5 GeV/c.

The TOF wall is followed by a 10.7 X_0 deep electromagnetic calorimeter comprising 'electromagnetic' CHORUS Pb–scintillating fibre modules [31], suitable for the rejection of electrons.

Table 4: Layout of the experiment; $+z$ denotes the downstream direction; distances in metres.

From	Until	$\langle z \rangle$	Detector
9.4	11.6		TPC solenoid flux return.
9.5	10.9		TPC active volume.
		10.0	Target centre (on beam axis, inside the TPC).
			The TPC is rotationally symmetric.
			Diameter 90 cm. Solenoidal field of 1.5 T.
			Measures r–ϕ and z coordinates. Particle identification by $\mathrm{d}E/\mathrm{d}x$.
11.9	12.4	12.15	Quadruplet of NOMAD drift chambers #1.
12.8	14.8	13.8	'Orsay' spectrometer magnet. with vertical dipole field.
			The Orsay spectrometer magnet has external dimensions
			3.2 m hor. $\times$ 2.2 m vert. $\times$ 1.7 m depth.
			The magnetic gap has at present dimensions
			2.2 m hor. $\times$ 0.7 m vert. $\times$ 1.7 m depth.
			Field integral after reconfiguration 1.0 Tm.
15.3	15.8	15.55	Quadruplet of NOMAD drift chambers #2.
16.0	18.5		Gas Cherenkov 2.8 m hor. $\times$ 1 m vert. entrance window
18.7	19.2	18.95	Quadruplet of NOMAD drift chambers #3 and #4.
19.2	19.7	19.45	Quadruplet of NOMAD drift chambers #5.
			The NOMAD drift chambers #3 and #4 are arranged as a pair
			(side by side, although separated by a gap of 1.5 m).
			Drift chamber #5 is centred. The wire directions
			are vertical, and $+5^{\mathrm{o}}$ and -5^{o} from vertical.
19.9	20.5	20.2	TOF walls.
			The TOF counter is a double-wall of scintillators of two sizes:
			$210 \times 21 \times 2$ cm^3 and $300 \times 21 \times 2$ cm^3.
			The central area covered is 460×300 cm^2
			(long counters) with two lateral pieces 140x210 cm^2 (short counters) to
			the left and right of the central piece. The two walls are staggered by
			10 cm with respect to each other to avoid loss of geometric efficiency.
20.7	23.1	21.9	Calorimeter = muon identifier.
			The calorimeter first consists of two layers of
			'electromagnetic' CHORUS Pb-fibre modules. Each layer has an
			area of 4.96 m hor. $\times$ 3.4 m vert.
			Then follow four layers of 10 cm of Fe,
			each followed alternately with a pair of quadruplets of
			NOMAD drift chambers, located side by side,
			and a wall of 'hadronic' CHORUS Pb–fibre modules.
			The NOMAD drift chambers cover an area of 6 m hor. $\times$ 3 m vert.
			The CHORUS Pb–fibre modules cover an area of
			8 m hor. $\times$ 3.6 m vert.
			The electromagnetic part comprises 6 cm of Pb ($= 10.7\ X_0$),
			good enough for vetoing electrons. The total number of
			interaction lengths of the calorimeter is 18 cm Pb + 40 cm Fe
			$= 3.4\ \lambda_{\mathrm{I}}$, suitable for muon identification.
			The calorimeter modules are all vertical. They are read
			out on either side, the vertical position is derived from
			the NOMAD drift chambers.

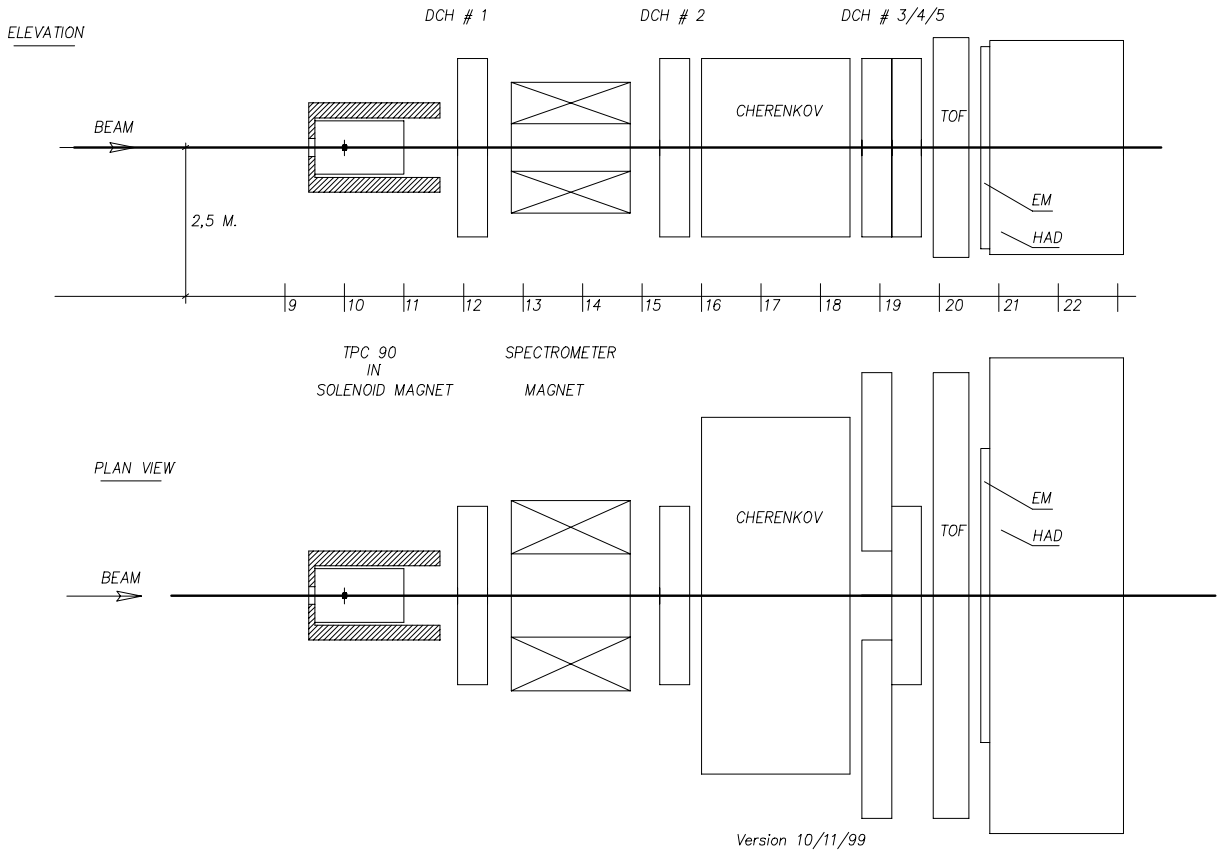

Figure 9: Plan and elevation views of the experiment. The target was arbitrarily placed at $z = 10$ m.

Then follow four layers of iron, each 10 cm thick. Each layer is followed alternately by a pair of quadruplets of NOMAD drift chambers, located side by side, or a plane of 'hadronic' CHORUS Pb–fibre modules. The total number of interaction lengths in both calorimeters is 3.4 $\lambda_{\rm I}$, suitable for muon identification (see Section 3.9).

3.3 Targets

A series of target materials will be used to cover a large range of elements. The choice of the target materials is influenced by practical considerations. Easily machined materials in solid form have the preference.

The primary set of measurements will be performed with 'thin' targets. Their thickness will be 2% of an interaction length. This value is chosen to minimize re-interactions in the target itself, while keeping a reasonable interaction rate. A list of target materials is given in Table 5. The thin targets have the shape of a disc with a diameter of 30 mm and a thickness between 8.1 and 1.9 mm.

A number of thick targets will be used with the primary aim of checking the simulation of re-interactions. The thickness of these targets will be of the order of one or two interaction lengths. The thickness for a one interaction length target is given in the third column of the table. The thick targets will look like rods with up to 407 mm length. It is expected that for the thick targets a smaller subset of materials will be used, e.g. C, Al, Cu and Pb.

Table 5: Set of envisaged targets. The second and third columns give the thickness of the 2% interaction length 'thin' version and the one interaction length 'thick' version respectively.

Material	thin target (cm)	thick target (cm)
Solid		
Be	0.81	40.70
C	0.76	38.00
Al	0.79	39.44
Cu	0.30	15.00
Sn	0.45	22.36
W	0.19	9.58
Pb	0.34	17.05
Cryogenic	(optional)	
H2	14.36	
D2	6.76	
N2	2.18	
O2	1.59	

The set of target materials can be modified to include Li, Ni, and Hg.

In a later stage, also cryogenic targets can be used, such as hydrogen, deuterium, oxygen and nitrogen. The construction of the target station with these target materials is much more complicated, and no design is yet available. The hydrogen target is useful to compare the results with earlier work. The use of the oxygen and nitrogen targets enables the direct measurement of production cross-sections needed for calculations of atmospheric neutrino fluxes. A deuterium target has been discussed in the framework of a recirculating proton scheme for the neutrino factory.

3.4 Time projection chamber

The TPC has a double role in this experiment. It is used to determine the momentum of tracks generated by charged particles over nearly the full solid angle, with emphasis on large-angle (including the backward-going) tracks. It serves also to identify pions, kaons and protons at low momenta. It is planned to re-utilize and suitably modify the ALEPH prototype TPC, the so-called TPC90, for the purposes of this experiment.

3.4.1 The ALEPH TPC90

The ALEPH TPC90 [9, 32] consisted of a solenoid magnet providing in pulsed mode (peak power consumption 1.2 MW) a uniform field of 1.2 T in a volume with 90 cm diameter and 1.75 m length; and of a cylindrical field cage closed with a high-voltage membrane on one side, and with a pad readout plane on the other. It was successfully operated for several years and laid the foundations for the design and construction of the large TPC which is ALEPH's central detector.

In order to re-utilize the TPC90, three major modifications are unavoidable: removing the downstream iron end-cap of the flux return while retaining the necessary homogeneity of the

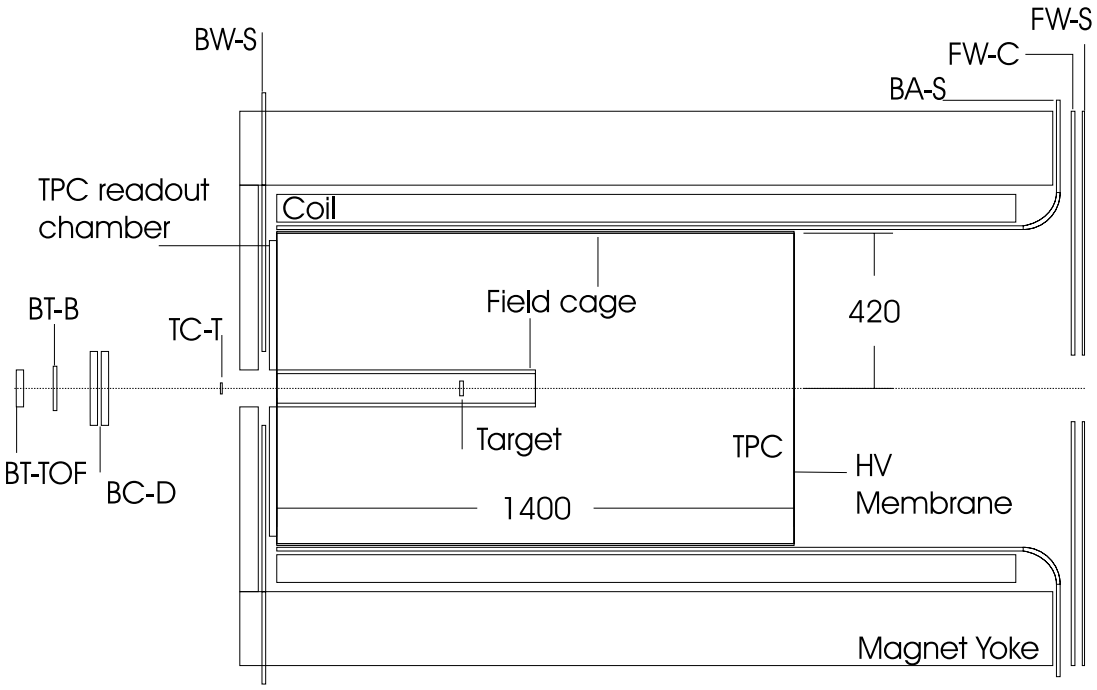

Figure 10: Side view of the TPC, the solenoidal magnet and the layout of the trigger detectors with the most downstream counters in the beam. The size of the active volume of the TPC is indicated in mm. Indicated are TC-T, the target defining scintillator; FW-S and FW-C, the forward scintillator and Cherenkov counters, respectively, and BW-S and BA-S, the backward and barrel scintillator planes, respectively. In the beam line the TOF counter BT-TOF and the beam defining scintillator BT-B are shown. BC-D is the most downstream beam chamber. TC-T defines the effective size of the target. The beam direction is from left to right.

solenoidal field inside the TPC volume; constructing a new readout plane with circular pad geometry; and adding a small cylindrical field cage which surrounds the target inside the TPC. Since building a field cage is now a well-understood technique at CERN, rebuilding the outer field cage is also envisaged. This would maximize the radius of the active TPC volume.

3.4.2 The solenoidal magnet

Simply removing the downstream iron end-cap of the flux return would lead to unacceptable radial field components and, as a consequence, distortions in the drift path of the charge towards the TPC end-plate (for optimal drifting, the electric and magnetic field vectors are parallel to each other). Therefore, the solenoidal coil as well as the cylindrical part of the iron flux return must be extended at the downstream end. A programme of mapping the field in the present magnet configuration, and of designing the new configuration with a view to minimizing radial field inhomogeneity, has been launched. The current overall layout of the experiment assumes that a protrusion of 60 cm beyond the TPC end-plate is adequate. CERN is expected to co-ordinate the modifications of the solenoidal magnet as well as to provide the field map measurements.

The upstream end of the solenoid magnet remains unchanged.

The coil has been routinely operated in pulsed mode at 1.2 T. Given the 400 ms spill of the CERN PS and a cycle time of 14.4 s, it is quite possible that the coil can be operated in pulsed

mode at 1.5 T. Tests will be performed to ascertain the feasibility of this goal, taking into account the limitations both from power dissipation and from magnetic field inhomogeneities due to saturation in the iron flux return.

3.4.3 The TPC mechanics

The new layout of the TPC is shown in Fig. 10. The active volume is a cylinder with 42 cm radius and 140 cm length, defined by the outer field cage. The drift field is parallel to the cylinder axis, and extends from a thin membrane at the downstream end of the TPC, held at -30 kV, to the read-out chamber which operates at ground potential. The upstream drift direction is motivated by minimizing the material which is in the way of secondary particles emanating from the target.

The target is located inside the TPC, 50 cm downstream of the read-out chamber, and held in position by a suitably designed insert which can be exchanged when a new target is installed. The insert fits into the inner field cage which has a radius of 5 cm. Thus the TPC is blind to forward track segments inside a 5 cm radius.

Between the outer field cage and the solenoidal coil is a radial space of 25 mm that is used by a cylindrical array of scintillators, which permits triggering on large-angle charged particles.

The design of the pad readout is guided by the knowledge gained with the ALEPH TPC:

- A pad plane with 6 mm (azimuthally) $\times$ 15 mm (radially) pads arranged in concentric circles between 7 cm and 40 cm radius, giving a total of $\sim$ 5000 pads. The pads are connected to preamplifiers (NA49 design) which are located as close as possible to the pads.
- A sense-wire/field-wire plane with octagonal symmetry 4 mm downstream of the pad plane. The wires are not read out.

3.4.4 TPC performance

The TPC is filled with 90% Argon and 10% methane. The drift velocity is saturated at 5 cm per μs, giving a TPC cycle time of 30 μs. It is therefore the slowest detector and limits the maximum rate of the incident beam, see section 4.

An 8-bit dynamic range of the pad readout is ample.

The pad design should comfortably permit an r–ϕ resolution of 300 μm per pad ring. The Gluckstern formula gives, with a magnetic field of 1.5 T and 21 samplings, a p_{T} resolution of

$$\Delta p_{\mathrm{T}}/p_{\mathrm{T}} = 0.033\ p_{\mathrm{T}}$$

Along the drift direction, a sampling every cm (corresponding to a 5 MHz clock frequency) is sufficient.

The greatest danger to the precision of measuring the momentum of tracks comes from residual inhomogeneities of the magnetic field. The safest way to control such problems is by using laser tracks, which have the added advantage that they not only calibrate the straightness of tracks but also permit the linearity of the analog pad readout to be ascertained.

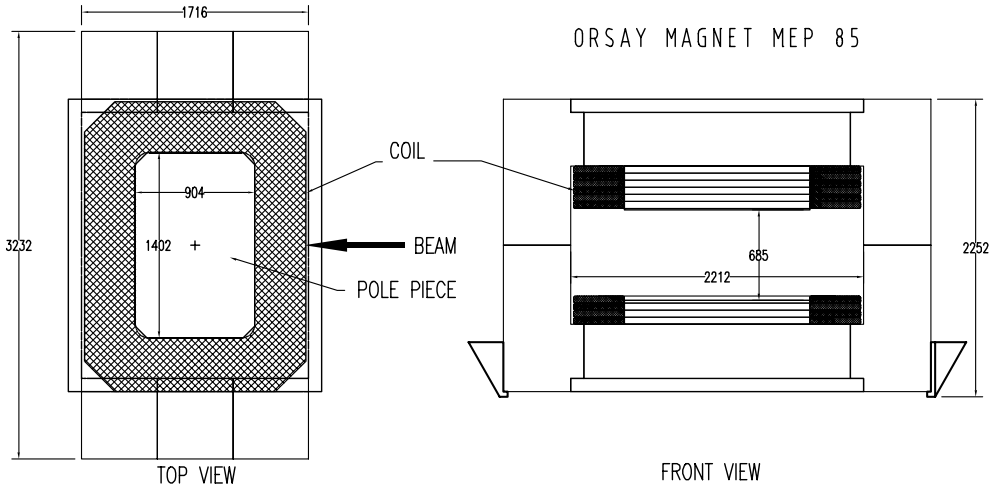

Figure 11: Top view and side view of the spectrometer magnet. All sizes are in mm.

It is envisaged that outside of run periods, the target insert will be replaced by an optical insert which brings in a laser beam and directs it into the active TPC volume by means of a set of prisms which sample different polar and, by rotation, different azimuthal angles. This calls for the optical transparency of the inner field cage at certain positions.

3.4.5 The TPC electronics

The TPC electronics is the single most demanding readout element. Every 200 ns a total of 5000 analog signals must be digitized into 8-bit words and preprocessed, over 30 μs, 1000 times per 400 ms spill, giving a *raw* data volume of 0.75 Gbyte. Zero suppression, which will reduce the instantaneous data volume by a factor of ~ 100, appears mandatory.

Although very demanding and at the forefront of technology, such readout problems have been solved already, notably by designs for the NA48 and ALICE experiments. Although the work toward a concrete design of this experiment's TPC readout is not finished, there is confidence that the problem can be solved within realistic time and cost limits.

3.5 Spectrometer magnet

The track momentum measurement in the TPC is complemented by the measurement in the downstream spectrometer. While the TPC magnet is mainly devoted to low-momentum and large-angle tracks, the downstream spectrometer measures high-momentum small-angle tracks.

The spectrometer magnet that we plan to use was built about 30 years ago at the Orsay laboratory and was previously used in PS and SPS hyperon experiments. It has a variable number of horizontal race-track coils providing a vertical field of up to 1.5 T over a gap of 0.7 m. The pole pieces measure 0.9 m $\times$ 1.4 m. For its previous high-momentum applications, the longer side (1.4 m) of the pole pieces was oriented parallel to the particle direction. For the proposed experiment a large angular acceptance is of prime importance, whereas a field integral of around 1 Tm is adequate. Therefore the orientation of the magnet will be changed. This orientation was already foreseen as an option at the time of construction of the magnet. It implies displacing the

vertical return yoke elements. In addition the water connections have to be renewed. Depending on the outcome of the magnetic field calculations, a number of coils will be removed, resulting in a larger vertical gap. It is estimated that four man-months of work will be needed for these modifications. CERN is expected to co-ordinate the modifications of the spectrometer magnet as well as to provide the detailed field-map measurements.

Figure 11 shows the spectrometer magnet as it will be used in the experiment. The gap height might be further increased by removing some of the coils. The total gap width is 2.2 m. The field is homogeneous within 10% over a total width of 1.8 m, dropping quickly towards the sides. The total depth of the magnet structure is 1.7 m. We plan to operate it at a field of 0.75 T, providing a field integral of 1.0 Tm. This gives a deflection angle of 60 mrad for 5 GeV/c particles. The operating values are 1600 A for a total power of 0.32 MW.

3.6 NOMAD drift chambers

The drift chambers were the active target of the NOMAD experiment and as such were more 'massive' than ordinary drift chambers. Each chamber consists of three gas gaps (8 mm) separated by 1.5 cm honeycomb-structured panels representing 2% of a radiation length for a complete chamber. The wire orientation in NOMAD was $+5°, 0°$ and $-5°$ with respect to the horizontal direction and the cell size is $\pm$ 3.2 cm. The field shaping was designed to allow easy switching from operation in a magnetic field (NOMAD conditions) to no magnetic field (this experiment). The gas mixture chosen in NOMAD was 60% ethane and 40% argon. To avoid the mandatory safety aspects related to this flammable gas mixture the chambers will be operated in a 90% argon – 5%CO_2 – 5%CH_4 gas mixture pending operational tests. The wire signals are fed to a preamplifier and a fast discriminator and then to a LeCroy 1876 TDC.

The typical efficiency of the chambers is 97%, most of the loss being due to the supporting rods used to maintain the 3 m long wires at the center of the gas gap. The number of dead channels (preamplifiers or HV problems) was less than 1% in NOMAD. The average space resolution reached 150 μm for normally incident particles, degrading to 700 μm for 45° tracks. The minimum track separation is around 1 mm. More details can be found in [7]. These chambers are available including preamplifiers, cables and TDCs. Parts of the gas distribution system will have to be reconstructed.

For this experiment the NOMAD chambers have to undergo only slight mechanical modifications. The small stereo angle (5°) was chosen with respect to the magnetic field direction. In this experiment the chambers should be turned by 90° to orientate the wires vertically. The mechanical structure used in NOMAD grouped four chambers (a module) together to ensure planar rigidity. This structure can easily be modified to provide suspension of the same four chambers with vertically oriented wires. These 12 active planes will then give good redundancy for tracking measurements just upstream and downstream of the spectrometer magnet. Concerning the chambers positioned between the Cherenkov and the TOF, the three modules staggered as in Fig. 9 are designed both to cover the whole TOF acceptance ($>$ 5 m horizontally) and to increase redundancy in the extreme parts of the central module.

The good resolution in NOMAD came as a result of a lengthy procedure of 'alignment' of the 6000 wires, making full use of the muon halo of the neutrino beam, thanks to the TDC 'memory' of 64 μs. The same should be possible with the muon halo of the hadron beam, thus requiring no special trigger.

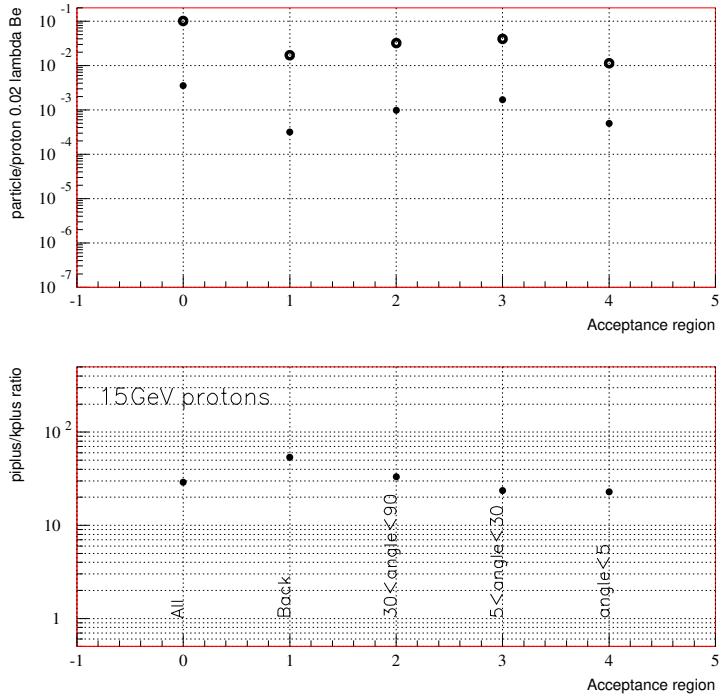

Figure 12: K^+ (closed circles) and π^+ (open circles) yields (top), and their ratio (bottom) for different angular acceptance regions.

3.7 Gas Cherenkov detector

At large incident proton energy, the secondary meson and proton momenta unavoidably increase, and the particle identification capabilities of the TOF and TPC have to be supplemented by another technique (Fig. 4). In addition to the proton/pion separation issue, the strange-particle contamination of the pion sample also increases. By simulation, the kaon contamination is more severe at large momenta of the secondaries, i.e. in the forward region, where the ratio K^+/π^+ is estimated to be about 5% (Fig. 12). In the same way, we can predict (Fig. 13) that 95% of the pions above 3 GeV/c are concentrated in the polar angle region $\theta < 200$ mrad, and therefore the 'large momentum' particle identification can be restricted to this domain: one obvious solution consists of using a gas Cherenkov detector of about 2.8 m width positioned downstream of the bending magnet. The vertical acceptance is nevertheless limited by the aperture of the magnetic element (70 cm).

A suitable gas for the radiator is C_4F_{10} (see Table 6): It is environmentally safe, non-flammable, has a low boiling point (room-temperature operation) and has well-understood behaviour from previous experiments. Its high refraction index allows the radiator to be operated at atmospheric pressure and in threshold mode.

With respect to a ring imaging detector, a threshold Cherenkov detector allows for a simpler design and construction: fewer photo-detector channels, no need of chromatic aberration control, larger tolerances for the optical system. The light collection can be implemented by using the well-known scheme of Al reflective mirrors: as reference, we will use the TASSO [33] design. In this set-up, a 'quality factor' of $N_0 = 110$ cm^{-1} has been reached with ordinary photomultipliers and Al mirrors (no coating) in Freon 114[1].

[1]Chlorofluorocarbons can no longer be used, and have to be substituted by equivalent perfluorocarbons.

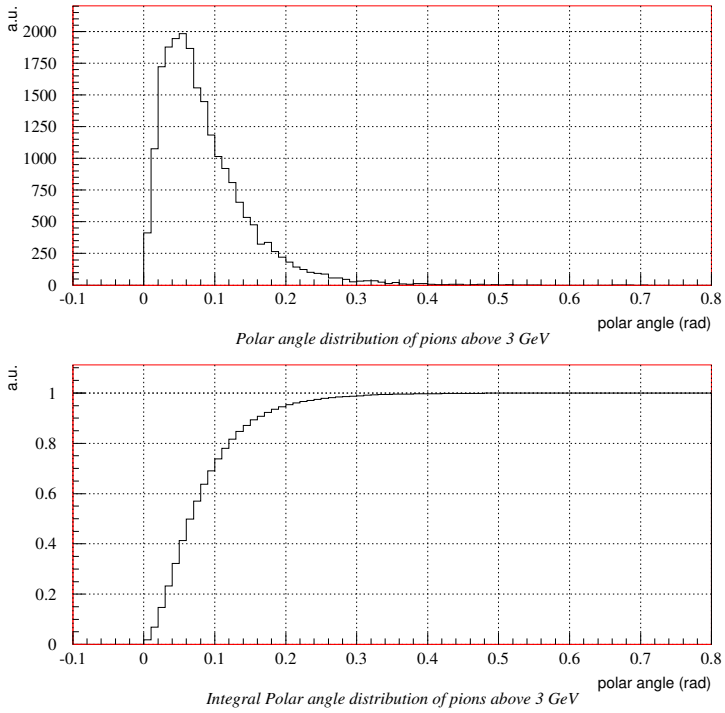

Figure 13: Angular distribution of positive pions with momentum larger than 3 GeV/c (top). The integral distribution is shown below.

Table 6: C_4F_{10} chemical/physical characteristics

Boiling point (°C)	-2
Molecular weight (g/mol)	238.0
$(n-1)\times 10^6$	1415
$\gamma_{\rm thr}$	18.8
Pion threshold (GeV/c)	2.6
Kaon threshold (GeV/c)	9.3
Proton threshold (GeV/c)	17.6
$\theta_c^{\rm max}$ (mrad)	53
$\mathrm{d}^2N/\mathrm{d}x\mathrm{d}E$ (photons/cm/eV)	1.04

The subdetector could be made by 16 identical modules with an input window of 35 × 50 cm^2, positioned symmetrically with respect to the horizontal plane to cover a surface of 280 × 100 cm^2 (Fig. 14). Each module contains a single mirror and a 5" photomultiplier. The mirror has an ellipsoidal shape with the photomultiplier and the target at focal points. Clearly, the magnetic fields will introduce distortions in the particle trajectories, resulting in a larger angular distribution of the particles entering one Cherenkov module. The actual angular acceptance of the single module (10° in the horizontal plane for the TASSO design) has to be optimized by a Monte Carlo study of the magnetic fields vs. mirror focal length. It has to be noted, however, that a larger angular acceptance can be reached by using 20" photomultipliers (commercially available) that have a photo-cathode surface 16 times larger. A minimum radiator depth of about 150 cm allows the detector to be operated in safe conditions, since about 40 photoelectrons can be expected for a relativistic particle (Fig. 15). The large photostatistics also allows pions and

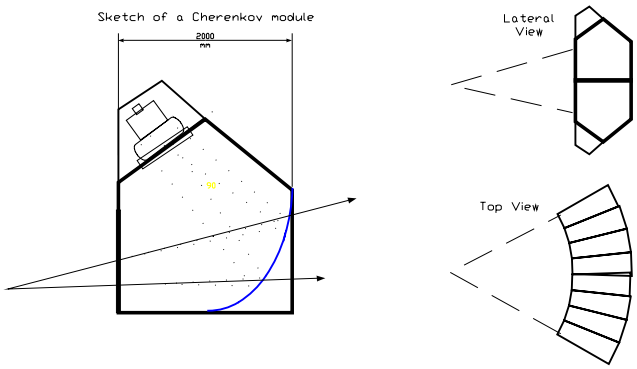

Figure 14: Sketch of a single Cherenkov detector module (left), and top and lateral view of the complete detector (right).

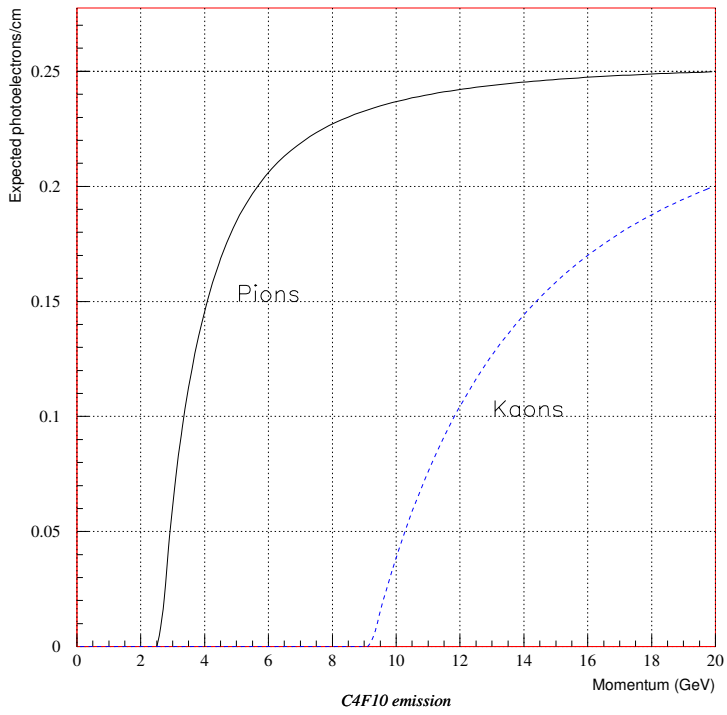

Figure 15: Photoelectron yield on photomultiplier measured in the TASSO Cherenkov detector normalized to 1 cm of radiator length. Both pion and kaon momentum curves are reported.

kaons to be discriminated above 9 GeV/c, by selecting on the intensity of the signals according to the momentum of the particle.

3.8 Time-of-flight wall

In the proposed design of a time-of-flight (TOF) system it is envisaged to use the scintillators that were used for the TOF system [34] of the Grenoble n–$\overline{\text{n}}$ experiment [35]. Part of these

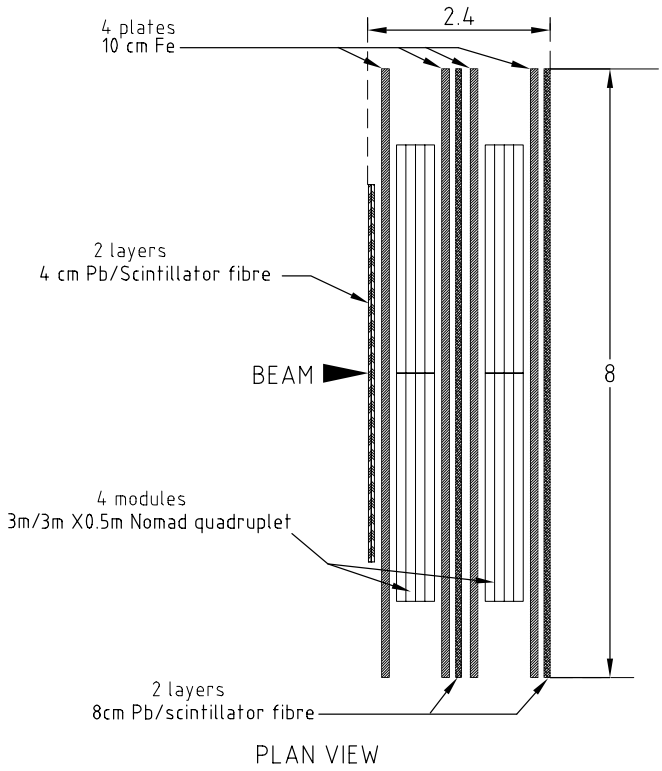

Figure 16: Conceptual layout in plan view of the muon identifier. Sizes are indicated in m.

scintillators were subsequently re-used in the NOMAD veto system [36].

The plastic scintillator used is NE110 manufactured by the former Nuclear Enterprise, UK. There are two types of counters: 28 slabs of $210 \times 21 \times 2$ cm^3 and 46 slabs of $300 \times 21 \times 2$ cm^3, all equipped with light guides and Philips XP2020 photomultipliers at both ends. The slabs are wrapped in a thin aluminum sheet and in black plastic. A small prism is glued to the centre of each scintillator. It allows connection to an optical fiber that can be used for an external timing monitoring system. Such a monitoring system, needed for this experiment, is no longer available and must be rebuilt. A specially designed mean-timer [37] can be used to build trigger signals for the experiment.

The time resolutions of the scintillator counters [34] were 270 and 320 ps, on average, for the 2.1 and 3.0 m long counters, respectively. The attenuation length was $\sim$ 350 cm. These performances were obtained with cosmic-ray measurements. Leading-edge discriminators were used and no correction for time walk effect was applied.

With these scintillation counters two walls of 20 m^2 can be equipped. The expected time resolution is already suitable to separate with 4σ pions from protons up to 3.5 GeV/c on the basis of 10 m flight path. We expect to improve the original resolution by using the amplitude measured by ADCs and combining the signals of the two consecutive planes. Also constant-fraction discriminators can be used. These techniques can help to improve the pion/kaon separation in the 1.5–3.0 GeV/c range and provide a useful overlap with the other particle identification methods.

3.9 Muon identifier

At low energies of the secondary pions and kaons the decay-in-flight probability will be important ($\sim$ 5% for pions and $\sim$ 40% for kaons of 2 GeV/c momentum).

Table 7: Parameter list of the beam and DAQ

Parameter	Estimated value
Event readout time	300 μs
Length of PS spill	400 ms
Maximum number of events per spill	1334
Length of super-cycle	14.4 s
Number of spills per day	6000
Maximum beam intensity (protons/spill)	3×10^5
Worst case π/beam particle	2×10^{-3}
Required statistics per setting	5×10^6
Number of settings	≈ 140

The decay of these particles produces the following effects:

- wrong p_{L} and p_{T} assigment;
- the decay of a pion in the Cherenkov detector will increase the TOF so producing a possible pion/kaon confusion.

Although these effects can be corrected on a statistical basis, muon identification on an event-by-event basis would be helpful also for solving problems of pattern recognition.

The quantitative importance of the above-mentioned effects is under study, as is the design of an efficient muon identifier. It must be recalled that the pion/muon separation is non-trivial as towards low-momentum pions increasingly look like muons in the passage through matter.

A possible design is shown in Fig. 16. The design is largely driven by the re-use of existing equipment. After a double-wall of the 4 cm thick CHORUS Pb–scintillating fibre modules (10 X_0) [31] that will also act as veto for electrons, a structure consisting of four times 10 cm Fe, interspersed alternately with a quadruplet of NOMAD drift chambers (side by side) and a wall of 8 cm thick CHORUS Pb–scintillating-fibre modules will permit hadrons to be separated from muons at the $\sim 90\%$ level.

The central part of the muon identifier is needed to detect muons in the incident beam. These have higher momenta than the particles produced in the interactions in the target. An extension of the muon identifier with a limited lateral size is envisaged making use of existing scintillator planes and iron pieces.

4 Trigger

The design of the trigger is driven by the capabilities of the data-acquisition system (DAQ), the performance and properties of the beam, the main features of the interactions to be studied and the required precision of the measurement envisaged. We will first make a rough survey of the conditions under which the trigger operates.

4.1 Running conditions

A list of parameters defining the running conditions is given in Table 7.

The secondary beam from the PS has a spill length of 400 ms with a repetition rate of one spill every super-cycle of 14.4 s. The intensity of the secondary beam varies depending on the momentum setting of the secondary beam line. By adjusting the collimators in the line and varying the production targets it will be possible to obtain particle rates of 10^5 to 3×10^5 for all energies. The beam on the target of the experiment will be focused to contain at least 90% of the intensity within a spot size of 10 mm diameter.

The optimum intensity of the secondary beam is limited by the occupancy of tracks in the TPC. The maximum drift time of the electrons in the TPC is 30 μs. The through-going beam particles traverse a dead zone in the TPC volume which is shadowed by the target cylinder. If the beam intensity is adjusted to give a maximum of 6000 interactions per spill (2% interaction length with 3×10^5 intensity), the overlap probability in the TPC is 0.6. It is expected that constraints on the interaction point provided by the beam chambers and combination with faster detectors downstream can resolve the ambiguities. In other detectors, the time windows are considerably smaller and the occupancy is negligible, except for the region traversed by the incident beam.

The number of random coincidences in the trigger should be kept at a reasonable level. With an intensity of 3×10^5 protons in a 4×10^2 ms spill time the random coincidence rate in a 10 ns trigger time window is less than 1%.

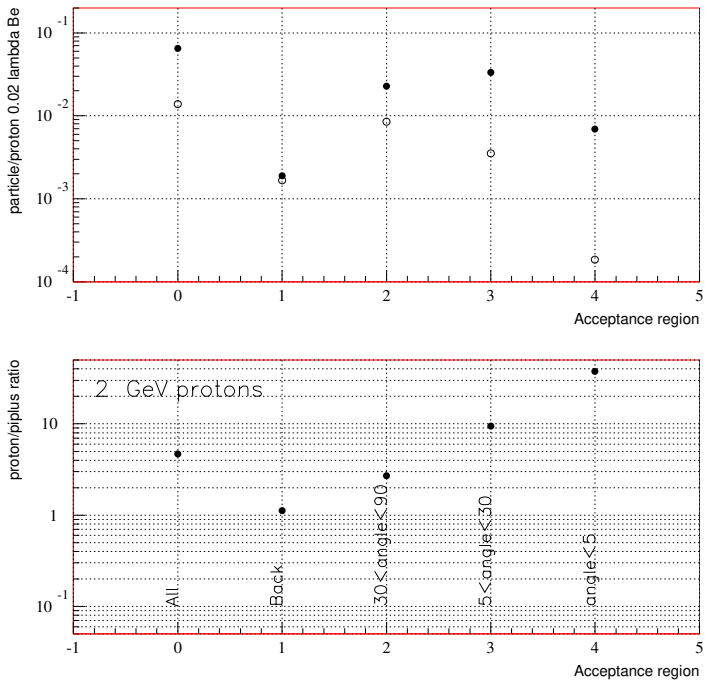

Figure 17: π^+ (open circles) and proton (closed circles) yields (top), and their ratio (bottom) at 2 GeV/c incident momentum for different angular acceptance regions.

The characteristics of the interactions vary greatly over the energy range of the experiment. At high energy, pion and proton production rates are roughly equal. Since both measurements are required, no selection on particle type will be needed in the trigger. At low-momentum settings

(below 4 GeV/c) the proton production dominates (Fig. 17). This effect is most marked in an angular range between 5 and 30 degrees. Therefore an additional trigger condition is required in this angular range to enrich the data with pion production.

To explore the two-dimensional phase space in transverse and longitudinal momentum with a statistical accuracy of 1% in the relevant area, 5 $\times 10^6$ events are required for each of the roughly 140 different settings (targets and momenta). To limit the measurement time to one year, one should aim at obtaining the statistics for each setting within one day, perhaps with the exception of the most difficult low-energy settings.

At low energy, the number of interaction triggers is low compared to the number of incoming beam particles. A decision dead time of 60 ns seems achievable, and gives a loss of 5% for 3 $\times 10^5$ incoming beam particles in a 400 ms spill.

The performance of the DAQ can only be determined with precision once a full design of all conversion electronics is available. It is estimated to be around 300 μs. Its effect on the number of events recorded is shown in Fig. 18.

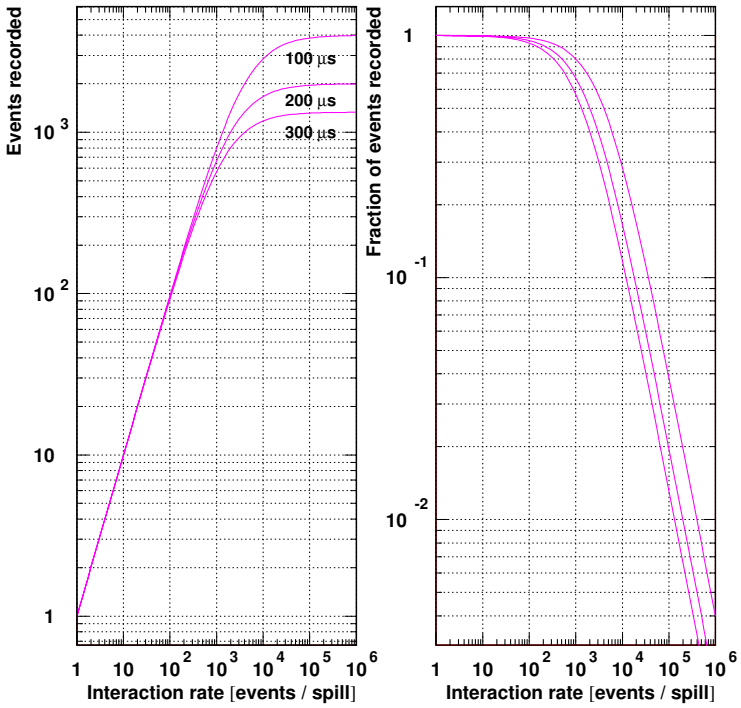

Figure 18: The effect of the read out time on the number of recorded events per spill (left) and the number of 'effectively used' triggers (right). The calculation is done for three values of the read out time (100, 200 and 300 μs). The spill duration is 400 ms.

4.2 Trigger layout

The trigger counters can be separated in three groups: the counters in the secondary beam line, near the TPC and downstream of the dipole magnet.

A large angular acceptance is achieved by combining a barrel-shaped system around the TPC volume with a planar system in the forward and backward direction. The various systems will have overlapping acceptances to allow a cross-check of the trigger efficiencies. The planar detectors have holes at the position of the beam spot to avoid triggering on non-interacting

beam particles. In low-energy incident beams up to 4 GeV/c it is important to distinguish pions from low-energy protons at the trigger level. Such suppression of proton triggers is only needed in a limited angular region (5 to 30 degrees). The use of a solid radiator such as quartz or lucite ensures the suppression of these protons. A thickness of 10 mm of quartz with a standard collection efficiency gives a comfortable number of 30 detected photoelectrons [38].

A series of scintillation counters is placed in the incident beam line (Fig. 10). A scintillation counter is used to give a precise timing for the TOF system **BT-TOF**. It has to be rather thick ($\sum$ 20 mm) for good timing resolution, and is therefore positioned far upstream of the target to avoid secondary particles faking a good trigger. A beam-defining scintillator is closer to the target. This counter is thin and has a circular shape of the size of the cylindrical free space around the target **BT-B**.

Beam chambers (**BC-U, BC-D**) are placed upstream and downstream of the scintillation counters, with the aim to measure the direction of the incoming beam within 1 mrad. The position resolution is about 1 mm projected onto the target. The precision of these detectors will make it possible to disentangle overlay beam tracks from the interacting beam particle.

A number of trigger elements are positioned inside the TPC magnet. These detectors are shown in Fig. 10.

The main trigger elements inside the TPC magnet are the scintillator layers **BA-S** and **BW-S**. The barrel shaped BA-S covers the large-angle region, partly including backward particles. It is read out with light-guides in the downstream direction. It gives a simple large-angle interaction trigger. The planar system of scintillators, BW-S, is fixed upstream of the TPC inside the Magnet yoke. The light is transported out of the barrel through the slits in the yoke with light-guides. A hole in this plane allows the beam to pass.

To trigger on forward produced particles, planar detectors are used immediately downstream of the magnet return yoke. A set of solid Cherenkov counters (**FW-C**) and scintillation counters (**FW-S**) is used. They cover at least the 90 cm diameter end-face of the TPC. The non-interacting beam particles pass through a $\sim$ 120 mm diameter hole in the middle of the detectors. A side view is given in Fig. 10. Light-guides carry the light sideways out of the fringe field of the solenoid. The Cherenkov has the function to discriminate protons from pions up to about 800 MeV/c, and is made of 10 mm quartz or lucite plate. It is only needed at low energies, and can be removed in higher-energy runs.

An array of planar scintillation detectors (**SA-S**) downstream of the dipole magnet defines triggers by detecting small-angle particles. These counters are located close to the TOF detectors shown in Fig. 9. They cover the diameter of the hole in the forward planar detectors with considerable overlap to allow for the effect of the bending field of the dipole magnet. Depending on the beam setting, a counter in the middle of the array is hit by the non-interacting beam particles and is not used in the coincidence. A selection of the TOF counters can be used for this function, perhaps complemented by a number of horizontal scintillator strips to improve the geometrical coverage at the centre, where the beam spot has to be blanked out.

4.3 Trigger conditions

In runs with thin targets the trigger requires a beam particle (BT-TOF $\times$ BT-B $\times$ TC-T) and a positive indication of an interaction, by defining an off-axis hit in any of the other scintillator planes. At low-energy running an additional Cherenkov signal is required in the forward region.

Table 8: Preliminary cost estimate of the data acquisition (in kCHF)

Item	Quantity	Unit price	TOTALS
VME crates	11	10	110
VME/PCI interfaces	11	5	55
DAQ-PCs	11	3	33
Local disk buffer	1	15	15
EVB/database PCs	5	3	15
Number crunching PCs	5	3	15
Control PCs	5	2	10
Monitoring PCs	5	2	10
Monitors	12	2	24
Network switches	2	4	8
Console switch	1	5	5
TOTAL			300

During data-taking with thick targets, most beam particles interact. It is not necessary to define sophisticated triggers, and a simple incoming beam trigger suffices. Also during operation with thin targets, it is important to have triggers defined with low-bias conditions. It is always foreseen to have a down-scaled incoming beam trigger and to have a trigger without the solid Cherenkov conditions with a lower down-scale factor. In the high-energy incoming beam settings, triggers without Cherenkov thresholds applied will be used without down-scaling.

5 Data acquisition and computing

5.1 Introduction

The data-acquisition system (DAQ) will read out the digitized signals from the ADCs and the TDCs. The DAQ will also take care of storage of the data in the proper sequence and format, the calibration of the detector and of the electronic readout chain, and the overall synchronization of the readout processes. It will also include slow control and data quality monitoring. The design aim for the DAQ is to keep the total dead time below 300 μs. A preliminary cost estimate is given in Table 8.

5.2 Readout and data volumes

An overview of the readout configuration is shown in Fig. 19. VME crates will be used wherever possible. The only exception to this rule will be the readout of the NOMAD drift chambers. The existing electronics in the FASTBUS standard will be re-used; in this case the FASTBUS crates will be interfaced to VME. Each VME crate will be connected to a readout PC via a VME–PCI interface.

64 channel ADC and TDC 9U VME modules will be used to read out the TOF system, the trigger system, the beam chambers and the gas Cherenkov detectors; these modules cannot be

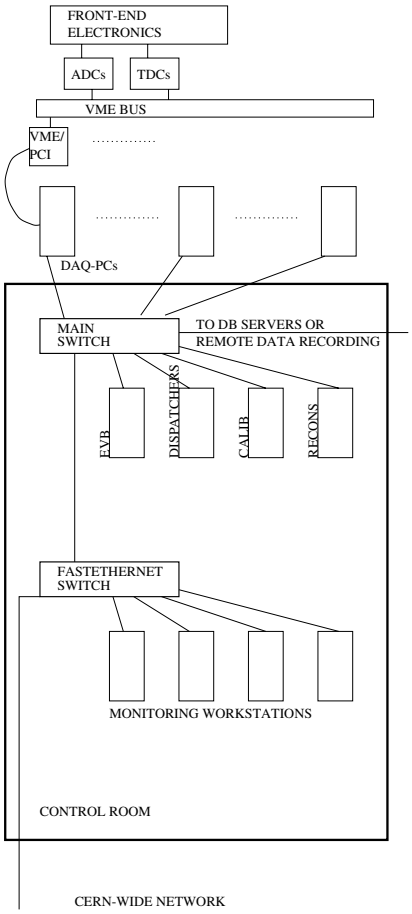

Figure 19: Schematic layout of data acquisition and networking.

recuperated from previous experiments and must be purchased.

All the necessary 96 channel FASTBUS TDC modules (LeCroy model 1876) needed for the NOMAD drift chambers are still available. These modules are equipped with an on-board 64 kB buffer memory and on-the-fly zero suppression [7].

A special case is the readout of the TPC, where we will use custom-made ADC modules developed in the framework of the ALICE TPC R&D programme. Up to 48 input channels per board may be sampled in parallel at 10 MHz with on-the-fly zero suppression and storage in a memory buffer [39]. We will operate these at 5 MHz. Approximately 100 modules will be needed to read out the TPC; of these, approximately 30 are already in existence and enquiries are being made to explore the possibility to borrow them, while the others have to be produced.

All the ADC and TDC modules will provide one data word per channel. All the data words will be 4 bytes long. Present tests of VME-PCI links show that the bandwidth in block transfer mode exceeds 10 Mbytes/s; conservatively assuming this data rate, keeping the readout time below 250 μs requires that no more than $\sim$ 620 words per VME crate have to be read out per event. These parameters have been used to determine the number of crates and DAQ-PCs that are necessary to build the DAQ system fulfilling the dead-time requirements.

The drift chamber system will be read out following the scheme already used in NOMAD: At each incoming trigger the zero suppression is performed by the TDC modules and the surviving hits stored in their memory buffer, which is then read out after the end of the spill. This ensures an almost dead-timeless operation of the drift chambers. The data volume produced by the TPC

is huge. Before any zero suppression, the TPC produces 150 samples per channel, corresponding to a total of 0.75 million samples. However, since the events have a low multiplicity, a large zero suppression factor can be achieved (a few 10^2) and a fast event-by-event readout (in less that $\sim$ 250 μs) will be possible. All the remaining detectors will be read out for each event without applying any zero suppression. All the data read out during the spill will be stored in the DAQ-PCs memory.

At the end of the spill all the data will be transferred in parallel to a dispatcher PC through Ethernet links. The dispatcher concept has already been successfully used by the CHORUS collaboration for DAQ environments, both inside and outside CERN [40]. The bandwidth of fast-Ethernet (100 Mbit/s) switches ensures that the data from the whole experiment ($\sim$ 26 Mbyte) will be transferred in $\sim$ 3 s. The spare time will be used by the DAQ-PCs to acquire calibration events.

Assuming 100% efficiency and 200 days running, the total yearly data volume would be approximately 30 Tbyte. Central recording at the computer centre of these data will be required. A disk buffer will be used to store the data of about four days running locally. Disk space for temporary data storage is also needed at the computer centre.

5.3 Network topology

The network will be organized around two Ethernet switches as in Fig. 19. The driving idea is to have a switched fast-Ethernet (100 Mbit/s) backbone dedicated to the critical tasks, and to screen anything else behind a second switch.

The readout PCs will be connected to the main switches to take advantage of the fastest possible network speed.

Direct connection on the main backbone is foreseen for all the PCs that require the highest possible throughput and the minimum possible latency. These machines will most likely be the readout processors, the dispatcher, the event builder (EVB), the calibration processors, the run controller and the file/database server.

To isolate the DAQ traffic which has the highest priority, the monitoring tasks will be run on workstations connected to the backbone via a fast-Ethernet switch. The link to the CERN-wide network will also be connected to the switches. Unnecessary traffic from the outside will have to be screened at the switch.

6 Performance of the spectrometer

A Monte Carlo simulation of the proposed experiment has been carried out using the GEANT [41] package, with the FLUKA [42] interface for the hadronic interactions. As examples of the expected performance, data with 2 GeV/c and 15 GeV/c protons impinging on a beryllium target with 2% λ_{I} thickness have been simulated.

The geometry and positioning of each of the subdetectors in the simulation is as described in Table 4 and as shown in Fig. 9. In a first stage of the simulation, tracking of all particles is carried out in each of the subdetectors with the position, momenta and identity of all the particles recorded. In a second stage, all particle detection effects such as momentum smearing and particle identification are simulated.

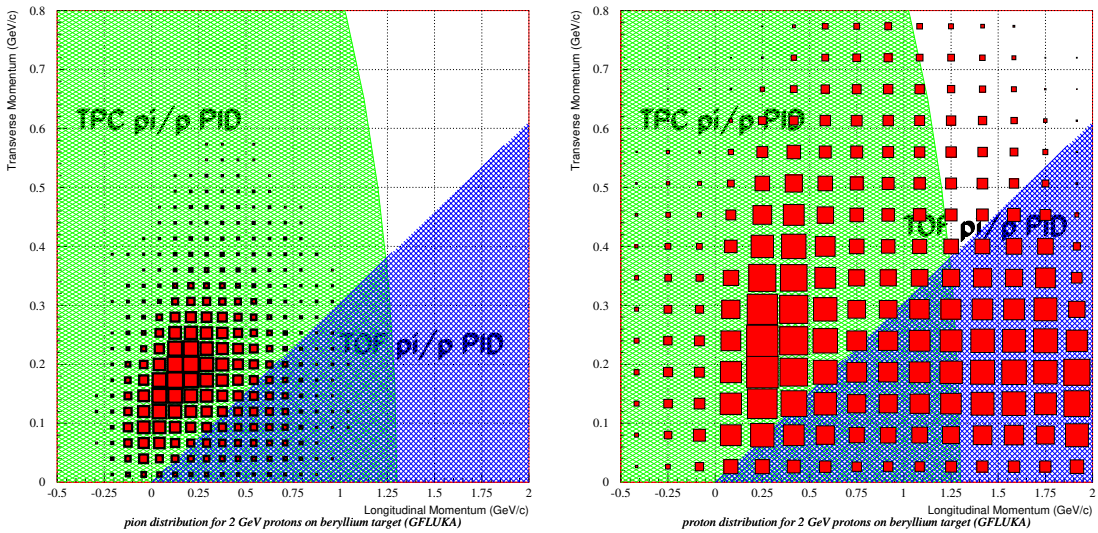

Figure 20: Production spectrum (by GEANT+FLUKA) $\mathrm{d}^2N/\mathrm{d}p_\mathrm{T}\,\mathrm{d}p_\mathrm{L}$ of (left) secondary pions and (right) secondary protons produced in collisions of protons of 2 GeV/c with a thin beryllium target. Superimposed are the areas of phase space expected to be covered by the π/p particle identification of the TPC and the TOF (at the 4σ level) in a simplified treatment.

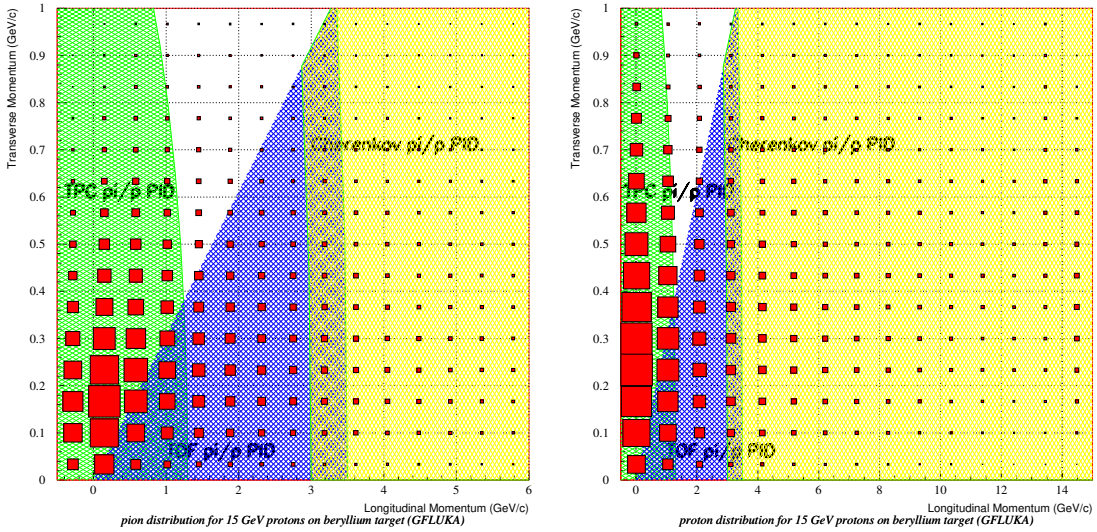

Figure 21: Production spectrum (by GEANT+FLUKA) $\mathrm{d}^2N/\mathrm{d}p_\mathrm{T}\,\mathrm{d}p_\mathrm{L}$ of (left) secondary pions and (right) secondary protons produced in collisions of protons of 15 GeV/c with a thin beryllium target. Superimposed are the areas of phase space expected to be covered by the π/p particle identification of the TPC and the TOF (at the 4σ level) in a simplified treatment. The combined analysis explained in the text gives better results.

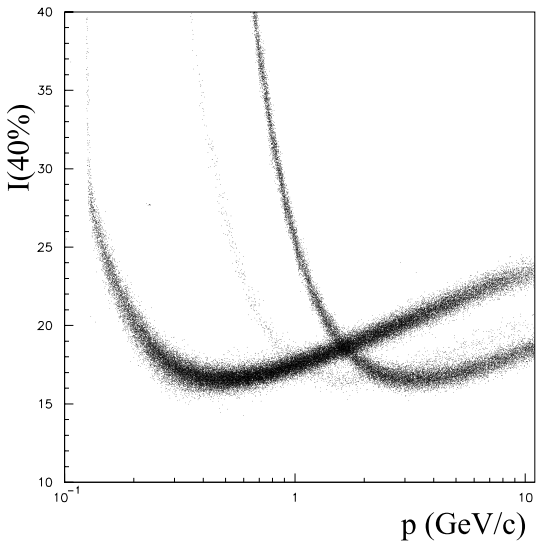

Figure 22: Truncated mean (40%) of the ionization loss (in arbitrary scale) of pions, kaons and protons in the TPC from 15 GeV/c protons on a Be target.

6.1 Momentum measurement

The momentum smearing inside the TPC is applied with the resolution given by the Gluckstern formula. The resolution of every r–ϕ measurement is assumed to be 300 μm, and the magnetic field is 1.2 T. A track is considered measured in the TPC when its projection onto the end-plate has a length greater than 15 cm.

For the momentum measurement in the spectrometer magnet, we use a quadruplet of NOMAD drift chambers before and after the magnetic volume. These drift chambers have a resolution of better than 250 μm, but they add 8% of a radiation length. In this case, the multiple scattering error dominates.

6.2 Particle Identification

To understand the particle identification capabilities of the TPC we assume a measurement of the ionization every cm. For the purpose of the simulation it is sufficient to assume that the gas is pure argon. To compute the ionization loss $I = \mathrm{d}E/\mathrm{d}x$ for each track we determine the truncated mean (at 40%) of the measurements. Fig. 22 shows the truncated mean (at 40 %) of the computed ionization loss $I = \mathrm{d}E/\mathrm{d}x$ for each track of the measurements.

The time of flight of a particle is calculated from the physical track length of a particle. It has been shown that a π/p separation can be achieved up to about 3.5 GeV/c at the 4σ level and a π/K separation up to about 2.5 GeV (at 2σ). The effective time resolution of the measurement of the TOF was assumed to be $\sim$ 300 ps.

We assume a very similar performance for the threshold Cherenkov counter to the performance of the TASSO Cherenkov detector [33]. The pion identification efficiency drops rapidly below 3 GeV/c towards the threshold at 2.5 GeV/c. Above 3 GeV/c, pions are identified with an efficiency close to 100%.

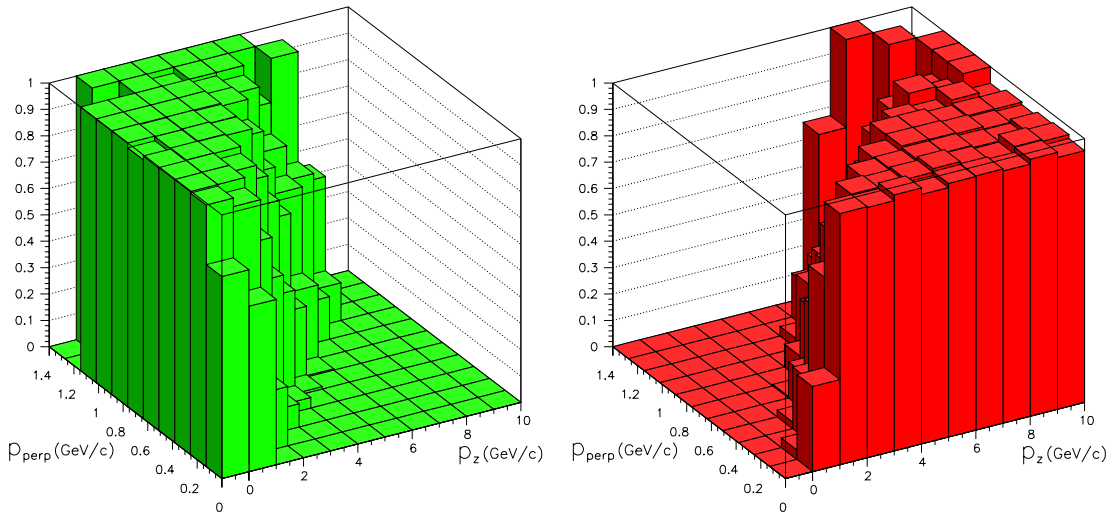

Figure 23: Acceptance of the detector for pions produced by a proton beam of 15 GeV/c incident momentum on Be measured in (left) the TPC and (right) the magnetic spectrometer.

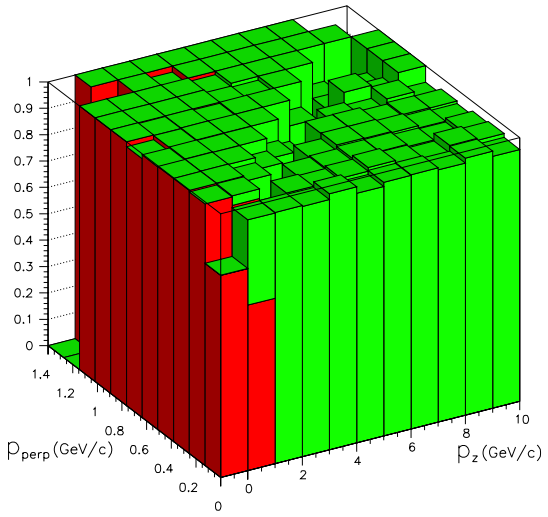

Figure 24: Combined acceptance for pions produced by a proton beam of 15 GeV/c incident momentum on Be measured either by the TPC or the magnetic spectrometer.

6.3 Results of the simulation

6.3.1 Geometrical acceptance

Figs. 20 and 21 show the distribution of events in the transverse–longitudinal momentum plane ($\mathrm{d}^2N/\mathrm{d}p_\mathrm{T}\ \mathrm{d}p_\mathrm{L}$) for the secondary pions and protons produced in the interactions with a thin beryllium target of 2 GeV/c and 15 GeV/c protons, respectively.

Overlayed on those plots one can see the approximate regions of parameter space covered by the π/p identification capabilities of the TPC and the TOF. At 2 GeV/c there is total particle

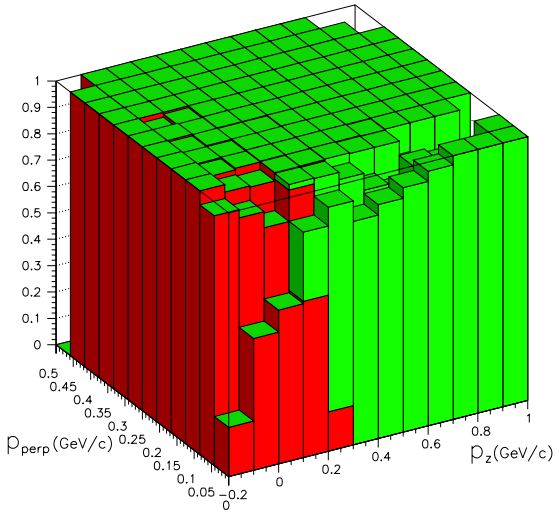

Figure 25: Combined acceptance for pions produced by a proton beam of 2 GeV/c incident momentum on Be measured either by the TPC or the magnetic spectrometer.

identification coverage for all pions and nearly all the protons.

At 15 GeV/c the π/p separation can also be achieved unambiguously for most of the phase space. Here a simplified particle identification in the TPC was assumed, limited to the momentum region below the crossing points of the ionization curves (Fig. 5). As will be demonstrated in section 6.3.3 good identification of pions can also be achieved with the dE/dx in this region. At this momentum there seems to be a small area between 2.5 and 3 GeV/c where π/K separation cannot be achieved unambiguously when one uses a particle identification in the TPC limited to the momentum region below the crossing points of the ionization curves. Sufficient identification can be achieved in this region on a statistical basis (section 6.3.3).

Fig. 23(left) shows a three-dimensional plot of the p_{L}–p_{T}-plane in which the third coordinate is the acceptance of the TPC for pions produced by 15 GeV/c incident protons. This is defined, for each event, as the number of pions which are triggered (that is, they hit at least one of the trigger scintillators) and tracked by the TPC (the projected length in the TPC end-plate must be longer than 15 cm), divided by the total number of produced pions. Fig. 23(right) shows the same plot for the magnetic spectrometer, while Fig. 24 shows the combined acceptance. This acceptance is purely geometrical. The acceptance of pions over the full phase space is almost 100%.

Similarly, one can show in Fig. 25 the same geometrical acceptance plot for pions from protons of 2 GeV/c. The geometrical coverage between the TPC and the rest of the magnetic spectrometer is nearly complete.

6.3.2 Particle identification efficiency

For each of the subdetectors with particle identification characteristics, we compute the probability that a particle is a pion, kaon and proton. For example, the probability that a particle is a pion in the TPC, $P^{\pi}_{\mathrm{TPC}}(I,p)$, is a function of the measured ionization and its momentum. We also define the pion identification efficiency as the number of correctly identified pions divided by the initial number of pions *tracked by the TPC* (so that we deconvolute the identification efficiency from the geometrical acceptance). We also calculate the kaon (proton) *relative* misidentification

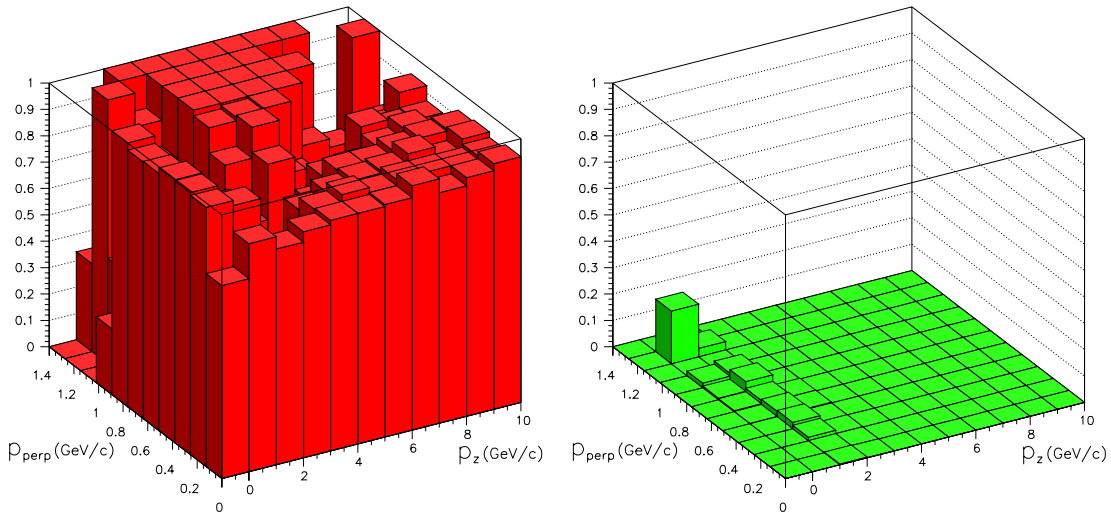

Figure 26: (left) Combined pion identification and geometrical acceptance of the detector and (right) global pion misidentification probability in bins of p_{L}, p_{T} from interactions of 15 GeV/c protons.

probabilities, as the number of kaons (protons) wrongly identified as pions divided by the initial number of kaons (protons) tracked by the TPC. Finally, we compute an *absolute* misidentification probability as the number of kaons plus the number of protons wrongly identified as pions divided by the *initial number of pions*. This latter quantity is a direct measure of the background in our sample of pions.

With a choice of $P^{\pi}_{\mathrm{TPC}}(I,p) > 0.6$, one keeps a pion identification efficiency of 92%, while reducing the absolute misidentification probability to about 0.4%.

Also defined is the probability that a particle is a pion, $P^{\pi}_{\mathrm{TOF}}(t,p)$, which depends on the time of flight (in ns) and its momentum. We repeat the same likelihood analysis with the TOF and with a choice of $P^{\pi}_{\mathrm{TOF}}(t,p) > 0.5$, one keeps a pion identification efficiency of 79%, while reducing the absolute misidentification probability to about 0.6%.

6.3.3 Combined Acceptance and efficiency

The combination of the geometrical acceptance and the particle identification efficiencies of the TPC, TOF and Cherenkov yields the combined acceptance. At this stage, we have applied very simple criteria, which we summarize as follows:

1. If the particle has $p > 3$ GeV/c and the track length in the Cherenkov is longer than 1 m we assume it can be identified in the Cherenkov with 100% efficiency. This is a good approximation of the efficiency of a threshold Cherenkov detector.

2. If the particle has $p < 3$ GeV/c and reaches the TOF, then it is identified as a pion if $P^{\pi}_{\mathrm{TOF}}(t,p) > 0.5$.

3. Else, if the particle has been tracked by the TPC, then it is identified as a pion if

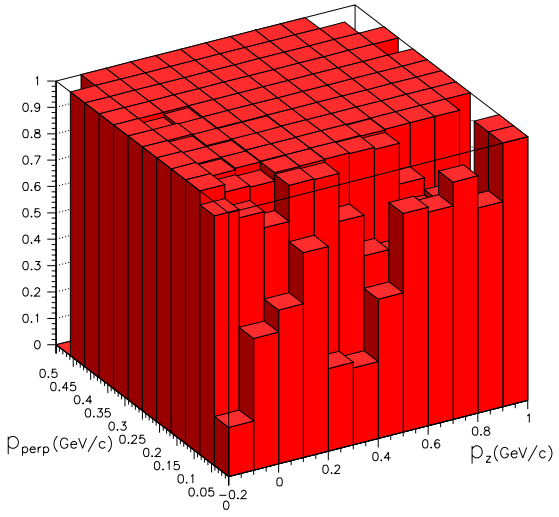

Figure 27: Combined pion identification and geometrical acceptance of the detector in bins of $p_{\rm L}$, $p_{\rm T}$ from interactions of 2 GeV/c protons.

$P^{\pi}_{\rm TPC}(t,p) > 0.6$.

Fig. 26 shows the combined pion acceptance plus identification efficiency as a function of $p_{\rm L}$, $p_{\rm T}$ and the pion misidentification probability as a function of the same variables from 15 GeV/c protons. The identification and measurement of pions is achieved with a high efficiency (90%) while maintaining the contamination from other particle types as low as 0.2 %.

For completeness we also show in Fig. 27 the combined pion acceptance plus identification efficiency as a function of $p_{\rm L}$, $p_{\rm T}$ for 2 GeV/c protons. The misidentification probability is totally negligible while the pion acceptance is very close to 100%.

To illustrate the performance of the apparatus we show in Fig. 28(a) the momentum distribution for pions (solid), protons (dashed) and kaons (dotted), *produced* by 15 GeV/c protons (i.e, the 'true' Monte Carlo distribution). The effect of the acceptance in these distributions can be seen in Fig. 28(b) while the effect of particle identification is shown in Fig. 28(c). The efficiency for signal and background is shown in Fig. 28(d). Coverage down to very low momenta is clearly obtained with the proposed apparatus. Even though the identification efficiency is somewhat reduced in the 1–3 GeV/c region, it is still possible to separate pions from other particles with a low background of misidentified particles.

As expected at 2 GeV/c incident proton momentum, the same analysis confirms that the efficiency for measurement and identification is practically 100%

7 Cost estimate

The estimated cost of constructing, installing and commissioning the experiment is given in Table 9. The cost of digitization electronics (ADCs and TDCs) and of cabling are reported separately. Some items can be reduced if more existing equipment can be re-used.

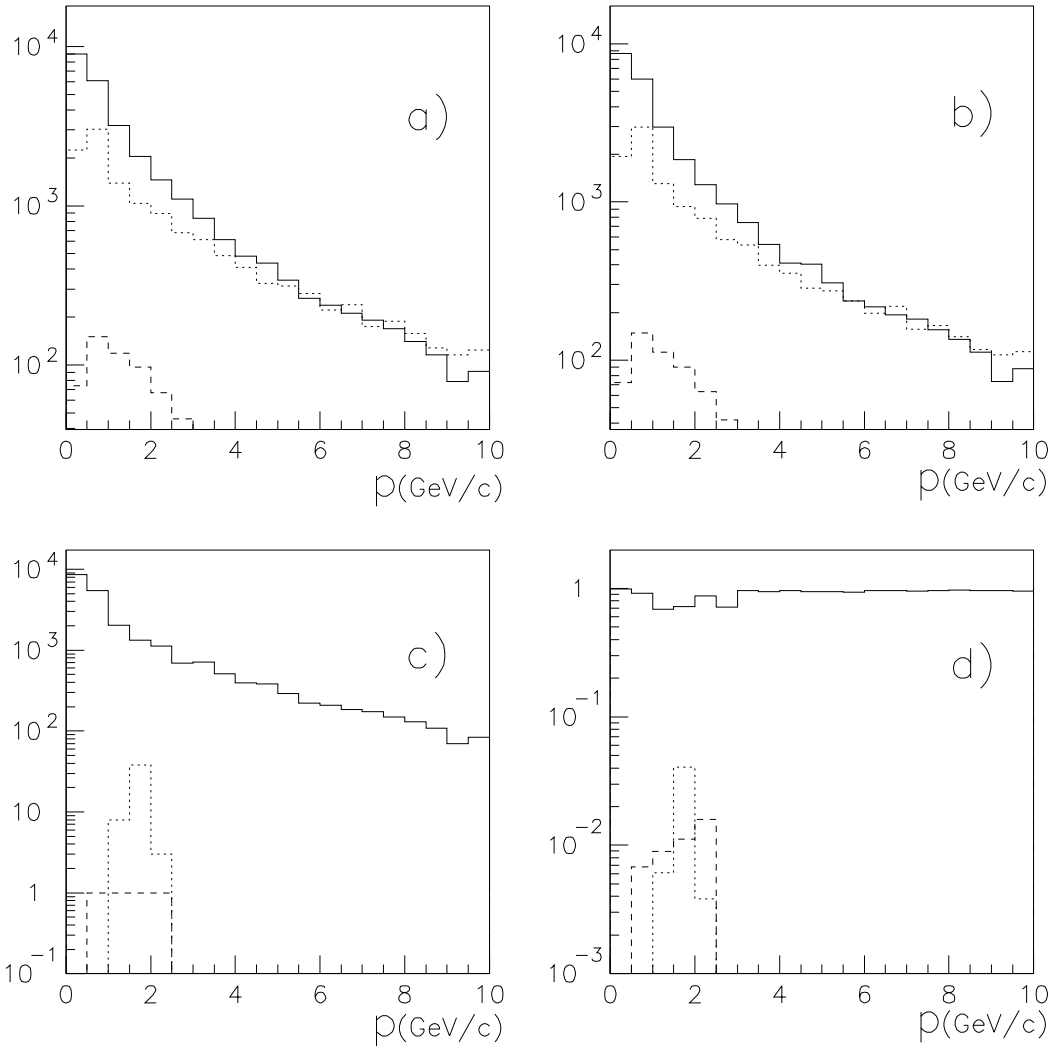

Figure 28: Momentum distribution for pions (solid line), kaons (dashed line) and protons (dotted line) produced in p–Be collisions at 15 GeV/c. (a) 'True' distribution, without convoluting with the geometrical acceptance and the particle identification; (b) the same distribution when the geometrical acceptance is included; (c) the same including the effect of particle identification (the background due to misidentified protons and kaons is shown with dotted and dashed lines respectively); and (d) final efficiency (acceptance and particle identification).

8 Schedule

From the point of view of the knowledge of the atmospheric flux, there is no specific timetable imposed, except that sooner is better than later.

From the point of view of the neutrino factory, there is an important choice to be made in the not–too–distant future. The two proposed extremes are a superconducting proton linac

Table 9: Cost estimate of the experiment construction (in kCHF)

Item	Cost	Digitization	Cables
Secondary beam upstream of the experiment's target (beam focus, particle id., T9 beam stopper)	50		
Beam chambers (mechanics, electronics)	10	24	4
Targets and associated mechanics support	50		
Trigger counters (including support structures, logic, distribution)	150	12	10
TPC field cages, pad readout chamber	300		
TPC readout (preamplifiers)	100	300	100
TPC solenoid magnet (coil extension, reshaping of flux return, installation)	100		
Spectrometer magnet (modification and installation)	60		
NOMAD drift chambers (mechanical supports, refurbishing)	150		
Gas distribution systems (for TPC and drift chambers)	100		
Gas Cherenkov (mechanical structure, mirrors, PMs, gas system)	350	2	
TOF walls (construction, mechanical supports, calibration system)	160	30	10
Muon identifier/ calorimeter (mechanical supports, installation)	100	90	30
Data acquisition (crates, processors, servers, work stations, slow control)	300		
Network connections	40		
Offline analysis infrastructure	50		
Experimental area (installation of infrastructure, access ways, cable trays, etc.)	50		
Experimental huts (installation incl. electronics racks and cooling)	100		
Electrical power distribution	50		
Safety equipment	100		
Installation manpower (three man-years, including a designer for six months)	300		
Subtotals	2670	458	154
Total		**3282**	

producing 2 GeV/c protons, or else a rapid-cycling synchrotron producing 16 GeV/c protons. If the decision is to be taken on the basis of measured data, they should become available as soon as possible.

Another constraint is the availability of the East Hall of the CERN PS for a large experiment, since the room is dedicated for later use by LHC experiments.

Therefore, the plan is to install and commission the experiment as rapidly as possible, with a

view to having a technical run in late 2000. The main data-taking period would be 2001. The option of a second data-taking period in 2002, with deuterium and helium running, should be kept open.

Acknowledgements

The authors wish to express their sincere thanks to all members of the Neutrino Factory Working Group for their advice and assistance: in particular to B. Autin, H. Haseroth, E. Keil and E.J.N. Wilson; and to R. Engel, T.K. Gaisser, J. Knapp, P. Lipari and A.A. Watson for valuable discussions on charged-particle cosmic rays. We are indebted to W. Blum for sharing his expertise of the TPC and to G. Mallot for the information on COMPASS. We greatly acknowledge the contributions from the staff of the PS division concerning information on the T9 beam parameters and infrastructure. We warmly thank the technical staff of the collaborating institutes who have contributed to the preparation of the proposal.

References

[1] Y. Fukuda et al. (SuperKamiokande Collaboration), Phys. Lett. **B433** (1998) 9; Phys. Rev. Lett. **81** (1998) 1562.

[2] T. Kajita, Nucl. Phys. **B77** (1999) 123.

[3] J.V. Allaby et al., CERN report 70–12 (1970).

[4] T. Eichten et al., Nucl. Phys. **B44**, (1972) 333.

[5] B. Cole et al., BNL Proposal 910 (1994), AGS propsal: "A Facility to Study Proton-nucleus and Heavy Ion Collisions using a Large Acceptance Detector with Particle Identification Capabilities."

[6] I. Chemakin et al., preprints nucl–ex/9902003 and nucl–ex/9902009 (1999).

[7] J. Altegoer et al. (NOMAD Collaboration), Nucl. Instrum. Meth. **A404** (1998) 96.

[8] E. Eskut et al. (CHORUS Collaboration), Nucl. Instrum. Meth. **A401** (1997) 7.

[9] S.R. Amendolia et al., Nucl. Instrum. Meth. **A252** (1986) 392.

[10] J.P. Riunaud, private communication.

[11] B. Autin et al., Prospective study of muon storage rings at CERN, CERN 99-02 (1999).

[12] D. Harris et al., Summary of detector/neutrino beam parameters. talk at Nufact'99 in Lyon, to be published in Nucl. Instrum. Meth.

[13] R. Palmer et al., Draft parameters of a neutrino factory, Muon Collider Note 46.

[14] R. Palmer, C. Johnson and E. Keil, A cost effective design for a neutrino factory. talk at Nufact'99 in Lyon, to be published in Nucl. Instrum. Meth.

[15] J. Collot et al., Particle production comparisons between MARS, FLUKA and E910, talk at Nufact'99 in Lyon, to be published in Nucl. Instrum. Meth.

[16] A. Blondel et al., A thin target scheme for the muon source, talk at Nufact'99 in Lyon, to be published in Nucl. Instrum. Meth.

[17] V. Agrawal et al. (Bartol group), Phys. Rev. **D53** (1996) 1314.

[18] M. Honda et al. (HKKM group), Phys. Rev. **D52** (1995) 4985.

[19] E.V. Bugaev and V.A. Naumov (BN group), Phys. Lett. **B232** (1989) 391.

[20] D. Perkins, Astrop. Phys. **2** (1994) 249.

[21] G. Battistoni et al., preprint hep–ph/9907408 (1999), to appear in Astrop. Phys.

[22] Y. Tserkovnyak et al., preprint hep–ph/9907450 (1999).

[23] T.K. Gaisser et al., Phys. Rev. **D54** (1996) 5578.

[24] T.K. Gaisser, talk given at the TAUP'99 Conference, Paris (France), September 1999.

[25] M. Honda, Nucl. Phys. **B77** (1999) 140.

[26] R. Bellotti et al. (MASS Collaboration), Phys. Rev. **D53** (1996) 35; R. Bellotti et al. (WiZard/MASS2 Collaboration), Phys. Rev. **D60** (1999) 052002.

[27] M. Boezio et al. (CAPRICE Collaboration), Ap. J. **518** (1999) 457.

[28] T. Sanuki et al. (BESS Collaboration), Proc. 26th Int. Conf. on Cosmic Rays, Salt Lake City (USA, August 1999), Vol. **3** (1999) 93.

[29] R. Engel, T.K. Gaisser and T. Stanev, Bartol preprint BA–99–73 (1999).

[30] T. Abbott et al., Phys. Rev. **D45** (1992) 3906.

[31] E. Di Capua et al., Nucl. Instrum. Meth. **A378** (1996) 221.

[32] W. Blum and L. Rolandi, *Particle detection with drift chambers*, Springer-Verlag.

[33] H. Burkhardt et al., (TASSO Collaboration), Nucl. Instrum. Meth. **184** (1981) 319.

[34] M. Baldo Ceolin et al., Nuovo Cim. **105A** (1992) 1679-1692.

[35] M. Baldo Ceolin et al., Z. Phys. **C63** (1994) 409-416.

[36] J. Altegoer et al. (NOMAD Collaboration), Nucl. Instrum. Meth. **A428** (1999) 299.

[37] A. Cavestro et al., Nucl. Instrum. Meth. **A305** (1991) 488-491.

[38] BaBar Collaboration, report SLAC–PUB–7428.

[39] J. Baechler et al., "Front-end electronics for the ALICE TPC detector", 4th Workshop on electronics for LHC experiments LEB98, INFN Rome, 21–25 September 1998; CERN–LHCC–98–36 (1998).

[40] R. Gurin and A. Maslennikov,
http://www-hep.fzu.cz/computing/HEPiX/HEPiX95/Overhead.html
CASPUR Consortium c/o Università "la Sapienza", Rome, Italy.

[41] GEANT 3.21, CERN Program Library, Long Writeup W5013.

[42] A Fassò et al., FLUKA 92, Proc. Workshop on Simulating Accelerator Radiation Environments, Santa Fe, 11-15 January 1993.